

## ABSTRACT

Title of thesis: MEMS CONVEYANCE: PIEZOELECTRIC  
ACTUATOR ARRAYS FOR  
RECONFIGURABLE RF CIRCUITS

Mary Claire Tellers, Master of Science 2015

Thesis directed by: Professor Sarah Bergbreiter  
Department of Mechanical Engineering

An array of piezoelectric cantilevers was designed, fabricated, and characterized for use as a micromanipulation surface in a reconfigurable RF circuit micro-factory. The project, known as RFactory, is an effort by the U.S. Army Research Laboratory to create environmentally adaptable, rapidly upgradeable RF systems. The RFactory actuator surface uses unimorph lead zirconate titanate cantilevers with metal posts at the tip that exaggerate the horizontal deflection produced by out-of-plane bending. The motion of a circuit component on the surface has been modeled and observed experimentally. By varying the waveform, voltage amplitude, and frequency of the drive signal, as well as the actuator length and width, the speed and precision of the motion can be controlled. From these characterization efforts, operating conditions that create speeds above 1 mm/s and low positional error ( $<200 \mu\text{m}$  after 5 mm translation) have been identified. Finally, full system RF reconfigurability has been demonstrated.

MEMS CONVEYANCE: PIEZOELECTRIC ACTUATOR ARRAY  
FOR RECONFIGURABLE RF CIRCUITS

by

Mary Tellers

Thesis submitted to the Faculty of the Graduate School of the  
University of Maryland, College Park in partial fulfillment  
of the requirements for the degree of  
Master's of Science  
2015

Advisory Committee:

Associate Professor Sarah Bergbreiter, Chair/Advisor

Professor Jaydev Desai

Professor Elisabeth Smela

© Copyright by  
Mary Claire Tellers  
2015

## Dedication

I dedicate this thesis to the memory of my friend and brother, Salifou Lansana Camara, who would have been incredibly proud to see me come this far, even if he wouldn't have understood my research. Truly good men are hard to find in the world, and he helped me make sense out of chaos and laughter out of tears. Here's to you, Slac.

## Acknowledgments

I would like to acknowledge all the support and assistance I have gotten from Army Research Laboratory employees and my University of Maryland laboratory.

I am greatly indebted to all the people who worked to create the actuator surfaces at the Army Research Laboratory. To Sarah Bedair and Iain Kierzewski, for their fabrication and processing support, I am very grateful. In the PiezoMEMS team, Joel Martin, Brian Power, and Steven Isaacson made the fabrication of the RFactory actuator surfaces possible. I would also like to thank Brett Piekarski for his support of both my project and my professional development. I would be remiss to not thank the Brain Trust: Ryan Rudy, Luz Sanchez, and Jon Puder. Ryan Rudy, in particular, has helped me immeasurably to figure out the inner workings of ARL, in addition to being a great collaborator on the RFactory system demonstrations.

At the University of Maryland, my lab group there has given me great feedback, provided constructive criticism, and supported me in papers and presentations. Dana, Ivan, Alexi, Simpson, and David—thank you so much! Even if you'd be happy to never hear the word jitter ever again. Ryan—a few embarrassing stories can never pay you back for your honest feedback, insane willingness to edit, and constructive advice. I'm going to miss you guys.

This work would not have been possible without Jeff Pulskamp, Ron Polcawich, and Sarah Bergbreiter. From the first vision of RFactory to the design of characterization experiments, Jeff has been a patient and knowledgeable guide and mentor in MEMS, piezoelectrics, and all things RF. My experience at ARL has

made me a better scientist and engineer, and I owe much of that to Jeff. Ron has also served as a guide to the world of research, but more than that, he jumped all the necessary hoops to get me the financial support that made this whole endeavor possible.

Sarah Bergbreiter has believed in me since the day I came by her office in 2009 and asked to learn more about MEMS. Despite the fact that my first experience in MEMS was less than stellar, her enthusiasm, curiosity, and impressive expertise has inspired me to continue my education in Mechanical Engineering. Although I think she feared I wouldn't come back to research as she wrote my Peace Corps recommendation letter, I think she always knew that research would pull me back in. I can't thank her enough for her unwavering support, for the effort she expended to bring me back to UMD, and for the push she's given me to go even further as a scientist. Few graduate students are lucky enough to have an advisor like Dr. Bergbreiter.

I would be remiss to not acknowledge the support of my family. Mom and Dad, thanks for all the advice and undying support since Day 1. Renee, thanks for letting me vent to you about grad school woes in all those phone calls. And Shaelyn and Dakota—thanks for making me feel like the “cool aunt” when I tell you about my tiny robots. I love you all!

# Table of Contents

List of Figures	vii
1 Introduction	1
1.1 Motivation	2
1.1.1 RFactory	2
1.1.2 System Overview	3
1.1.3 Actuator Surface	6
1.2 Literature Review	8
1.2.1 Reconfigurable RF Circuits	8
1.2.1.1 BAE Systems	8
1.2.1.2 Northrop Grumman	9
1.2.2 Micromanipulation	9
1.2.2.1 Electro-thermal Actuators	10
1.2.2.2 Electrostatic Actuators	11
1.2.2.3 Distributed Air-flow Actuation	13
1.2.2.4 Diamagnetic Levitation	14
1.2.2.5 Piezoelectric MEMS Actuators	15
1.3 Goals and Scope	16
1.4 Organization of the Thesis	18
2 Design and Modeling	20
2.1 Design of the Actuator Surface	20
2.1.1 Quasi-static model	21
2.1.2 Multi-physics Dynamic Model	24
2.1.3 Array configurations	30
2.1.4 Fabrication	31
3 Testing and Characterization	34
3.1 Metrics	34
3.2 Experimental Procedure	36
3.2.1 Measuring Experimental Data	37
3.2.2 Applied Signals	39

3.3	Waveform Results . . . . .	42
3.4	Voltage Amplitude Results . . . . .	47
3.5	Frequency Results . . . . .	51
3.6	Actuator Length and Width Results . . . . .	55
	3.6.1 Length . . . . .	55
	3.6.2 Width . . . . .	57
3.7	Technical Challenges . . . . .	59
	3.7.1 Side Contact . . . . .	59
	3.7.2 Post Height Variation . . . . .	59
3.8	Jitter Improvement . . . . .	61
3.9	RFactory System Demonstration . . . . .	63
4	Conclusions and Future Work	66
A	MATLAB Motion Tracking Code	70
	Bibliography	75

## List of Figures

1.1	RFactory is composed of an electrical interconnect surface, RF components resting on a MEMS actuator surface, and a bulk piezoelectric actuator that raises and lowers the RF components into and out of electrical connection with the interconnect substrate. . . . .	4
1.2	Schematic of RFactory reconfiguration . . . . .	5
1.3	Single Actuator Illustration . . . . .	7
1.4	Actuator configurations . . . . .	7
1.5	Insertion losses in a generic switch matrix system. . . . .	10
1.6	Thermal MEMS ciliary actuators . . . . .	12
1.7	Combined electro-thermal and electrostatic actuator . . . . .	13
1.8	Diamagnetic micromanipulators . . . . .	14
1.9	Converse piezoelectric effect . . . . .	16
2.1	Unit actuator of RFactory actuator surface . . . . .	21
2.2	Horizontal displacement caused by cantilever angular deflection . . . . .	21
2.3	Schematic of moment applied to the actuator . . . . .	22
2.4	Velocity response to actuator length and width . . . . .	23
2.5	Actuator-component FEA geometry . . . . .	26
2.6	Actuator-component mode used in dynamic model . . . . .	27
2.7	Actuator-component mode not used in dynamic model . . . . .	28
2.8	Modeled actuator and chip trajectories . . . . .	29
2.9	Examples of model predictions . . . . .	30
2.10	Actuator Array Layouts . . . . .	31
2.11	Fabrication sequence for RFactory actuator surface . . . . .	32
2.12	SEM image of 1D array . . . . .	33
3.1	Jitter Diagram . . . . .	36
3.2	Experimental set-up . . . . .	38
3.3	MATLAB motion tracking . . . . .	39
3.4	The on-axis velocity response of ramp, sine, and square wave driving signals shows that the highest velocities are achieved by square waves. Sine and ramp waves show improved speeds above 500 Hz. All devices used in waveform testing are 52 $\mu\text{m}$ long and 16 $\mu\text{m}$ wide. . . . .	43

3.5	An overview of the jitter performance of the various waveforms shows very high and variable jitter values for the sine wave compared to the other waveforms, especially below 500 Hz. . . . .	44
3.6	Angular jitter values for ramp and square waves. . . . .	44
3.7	Velocity response to ramp wave symmetry variation . . . . .	45
3.8	Jitter response to ramp wave symmetry variation . . . . .	46
3.9	Quasi-static model and symmetry response . . . . .	47
3.10	Velocity response to voltage amplitude variation . . . . .	48
3.11	The jitter response to voltage amplitude variation shows a good region of operation between 5 V and 8 V, as well as at 10 V. The discrepancy at 9 V is likely due to issues placing the chip consistently on the surface. . . . .	49
3.12	Quasi-static model comparison for voltage amplitude . . . . .	50
3.13	Velocity response to frequency variation . . . . .	52
3.14	Jitter response to frequency variation . . . . .	53
3.15	Quasi-static model of frequency response . . . . .	53
3.16	Multi-physics dynamic model compared to experimental data . . . . .	54
3.17	Impact of actuator length on velocity . . . . .	56
3.18	Impact of actuator length on jitter value . . . . .	57
3.19	Impact of actuator width on velocity . . . . .	58
3.20	Impact of actuator width on jitter values . . . . .	58
3.21	Side Contact . . . . .	60
3.22	This SEM of a Gen. 1 device's posts shows over-etch of the metal at the bottom and mushrooming at the top. . . . .	61
3.23	Jitter progress . . . . .	62
3.24	RFactory Assembly . . . . .	64
3.25	DC reconfigurability demonstration . . . . .	64
3.26	RF reconfigurability . . . . .	65
3.27	Verification of RF filtering . . . . .	65

## Chapter 1: Introduction

MEMS micromanipulation surfaces have been recognized for their potential utility since the 1990s as parts sorters, microassembly structures, and in micro-robotics [1]. The ability to position many milli- and microscale parts can be used in applications from manufacturing to bench-level testing. One potential application is in reconfigurable circuits, like those proposed by the “RFactory” project. RFactory aims to create reconfigurable radio frequency (RF) circuits, and one key requirement for this project is small-scale, low power, precise manipulation of micro- and milli-scale parts. In the course of characterizing the actuator array designed for the RFactory project, the principle of operation has been defined and high-quality operating conditions have been identified and employed to provide system-level demonstrations. The actuator array has developed from a poorly understood prototype system capable of only one direction of translation into a well-defined, reliable system capable of motion up to two bi-directional translational degrees-of-freedom (DOF) and rotation.

## 1.1 Motivation

### 1.1.1 RFactory

Traditional high performance RF integrated circuits (ICs) rely on a lengthy design process to achieve optimized designs for specific applications. The future of cognitive RF electronics relies on the ability of systems and circuits to be programmed, reconfigured, and/or adapt their functionality in response to dynamic spectral environments and requirements [2,3]. To obtain “application flexible” ICs, reconfigurable circuits have been proposed, primarily RF field programmable gate arrays (RF-FPGAs) that would reconfigure hard-wired circuit components through switching networks [4, 5]. An alternative approach, called “RFactory,” has been proposed by the U.S. Army Research Laboratory. RFactory is a motion-enabled microfactory that intends to bring adaptability and rapid component upgradeability to RF circuits. The intended applications of RFactory are consistent with the goals of the DARPA Adaptive RF Technology (ART) program [6], the same program that supports several RF-FPGA projects [4, 5]. RFactory aims to create adaptable electronics through reconfigurable circuits that offer insertion losses less than 3 dB with up to ten components in series, reconfigurability within seconds, and component updates in the field.

The actuator surface described in this thesis was developed to best suit the requirements of the RFactory system. For system power autonomy and rapid reconfigurability, RFactory requires a power draw of less than 1 mW and moderately high

Table 1.1: Project objectives for the RFactory actuator surface.

Phase 1 Objectives	
Positional Accuracy	
On-axis Translational Error ( $\mu\text{m}$ )	<100 $\mu\text{m}$ after 5 mm displacement
Off-axis Translational Error ( $\mu\text{m}$ )	<200 $\mu\text{m}$ after 5 mm displacement
Rotational Error (degrees)	<10 after 5 mm displacement
Speed	
Translation (mm/s)	>1
Rotation (RPM)	>60

speed actuation in the range of millimeters per second. Positioning and speed goals were set to ensure electrical contact resistance of  $<1 \Omega$  and reconfiguration within seconds. Table 1.1 outlines the project objectives of RFactory’s actuator surface. Additionally, the actuation mechanism has to be constrained to a 5 cm by 5 cm by 1 cm volume so that it can be integrated into the full system seen in Figure 1.1. These design goals led to material, actuator design, and actuator configuration choices.

### 1.1.2 System Overview

RFactory acts as a circuit factory, as shown in Figure 1.1. A die-level or packaged RF circuit component, such as a filter or an amplifier, is selected and placed on an active surface, which transports the chip to the designated location. Once in place, a Cedrat APA120S bulk piezoelectric actuator pushes components on the active surface into contact with an electrical routing surface through the use of

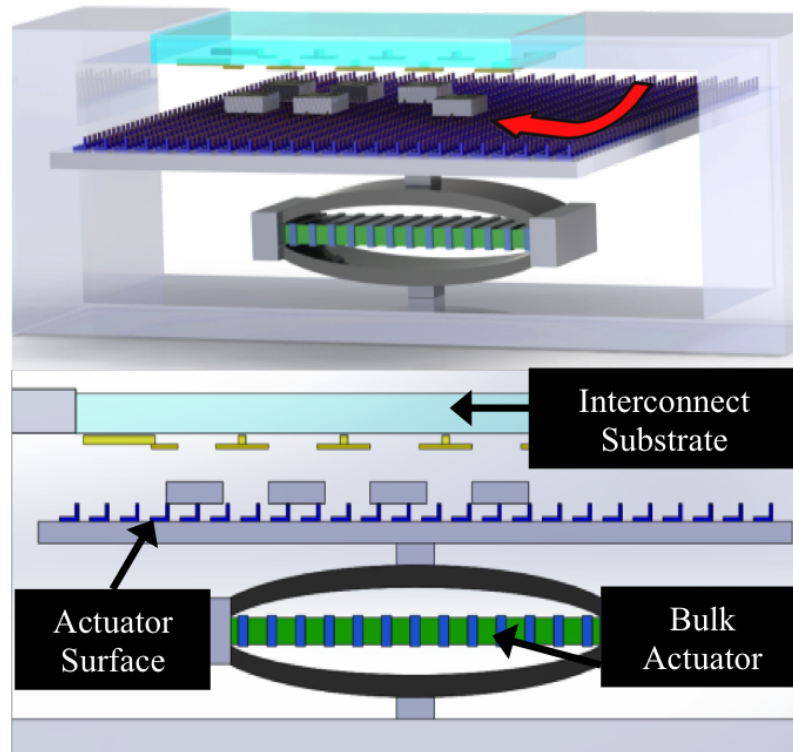


Figure 1.1: RFactory is composed of an electrical interconnect surface, RF components resting on a MEMS actuator surface, and a bulk piezoelectric actuator that raises and lowers the RF components into and out of electrical connection with the interconnect substrate.

compliant cantilevers. This substrate features an array of mechanically compliant contacts and transmission lines that permits chips to be electrically connected. As necessary, the bulk piezoelectric actuator can be lowered, allowing rearrangement, addition, or removal of components as desired. Figure 1.2 demonstrates what RFactory looks like before and after reconfiguration. The current demonstration-level RFactory system uses pre-selected component chips and open-loop control.

Similar to a circuit simulator like Agilent’s Advanced Design System (ADS),

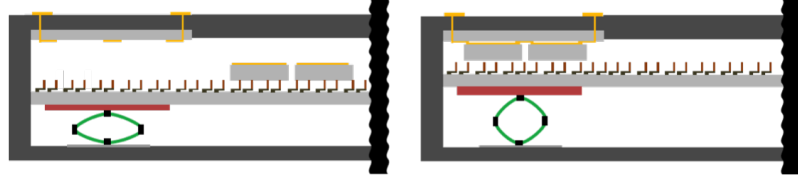


Figure 1.2: Left: Open configuration of RFactory. Right: Closed configuration of RFactory. Note how the components have been moved into position and the bulk piezoelectric actuator has pushed the actuator surface up so the components are in contact with the compliant contacts.

RFactory can demonstrate system performance of several circuits without having to build a hard-wired circuit for each layout. One advantage of RFactory is that its components are fabrication and technology agnostic. Additionally, RFactory reduces transmission line losses and eliminates the need for large switching networks by physically locating components close to the components they connect to. Transmission line losses greater than 0.5 dB/mm at 20 GHz are considered to be high, and the extra wiring length due to routing around hard-wired components leads to significant attenuation even if low-loss transmission lines ( $<0.6$  dB/mm at 50 GHz) are used [7]. Also, RFactory allows a circuit to be upgraded on a component level. As microfabrication technology improves, RFactory can stay on the cutting edge simply by substituting higher performing components as they are developed. When a component fails in RFactory, replacements can be made in seconds. RFactory enables simple heterogeneous integration, reduces switch counts and transmission line losses from conventional reconfigurable circuit approaches, and facilitates system and component upgradability.

### 1.1.3 Actuator Surface

When the RFactory system was first conceived, it was evident that a micro-manipulation surface capable of precisely maneuvering RF components would be required for the system to succeed. When open-loop control is used, precision and repeatability in the actuator surface lead to reduced contact resistance variation, more flexibility in component size selection, and overall electronic performance. When closed-loop control is used, the precision and repeatability of the actuator surface provide a more well-defined model for controller design. These requirements were quantified in the RFactory project proposal by limiting motion error to 100  $\mu\text{m}$  on-axis, 200  $\mu\text{m}$  off-axis and  $10^\circ$  of rotation after 5 mm of travel.

In addition to precision and repeatability, the actuator surface also needs to be fast and low power. Speed is required for rapid reconfigurability. In a scenario where a particular frequency is being jammed, the radio may have just a few seconds to reconfigure to a new frequency in order to maintain communications capabilities [3]. Low power is required for future system power autonomy and a target power for the actuator surface is 1 mW.

The development of the RFactory actuator surface (AS) stems from the use of lead zirconate titanate (PZT) in microrobotic legs [8]. The basic actuator unit for RFactory was derived from the microrobotic PZT work: a unimorph piezoelectric cantilever with a metal post at the tip to exaggerate the horizontal deflection of the tip, seen in Figure 1.3. The cantilevers can be arrayed in several configurations depending on the motion desired. Opposite-facing arrays create forward and reverse

motion, and a unit cell of up, down, left, and right actuators can create motion with two bi-directional translational DOF, shown in Figure 1.4 on the left. Additionally, coupled actuators create rotation in an array like the one shown in Figure 1.4 on the right. The RFactory actuator surface is designed to produce microscale motion in up to two bi-directional translational DOF and rotation.

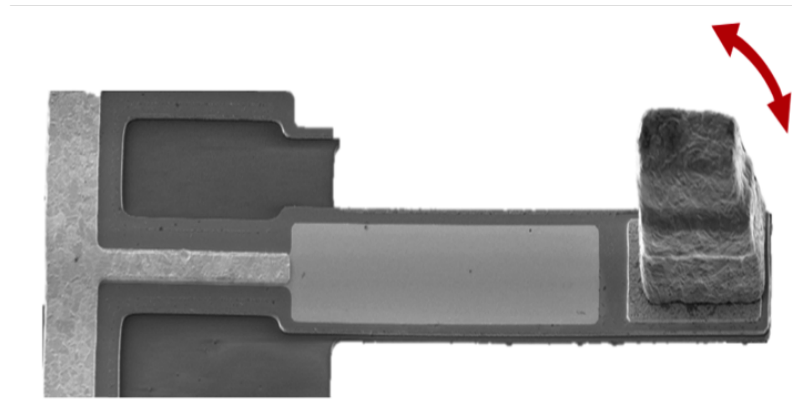


Figure 1.3: This scanning electron micrograph (SEM) has been edited to isolate a single actuator. The red arrow indicates how it bends out of plane when a voltage is applied across the thickness of the cantilever.

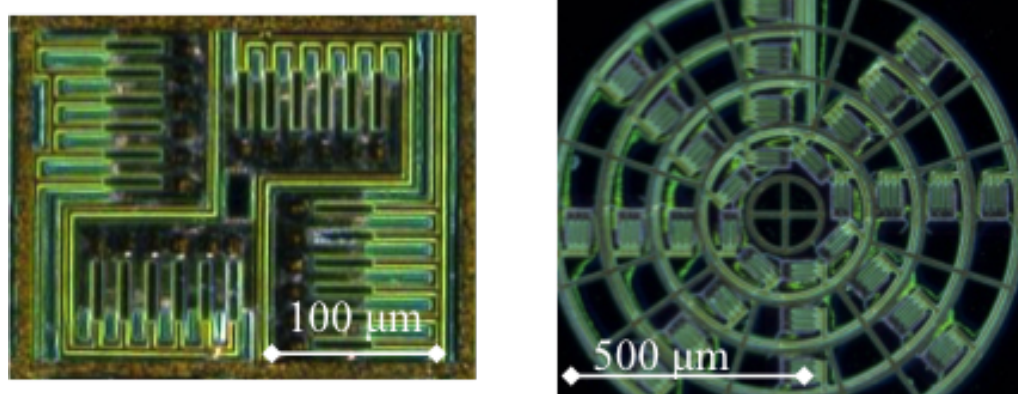


Figure 1.4: Left: Orthogonally arrayed actuator rows create bi-directional translation in both X and Y. Right: Actuators arrayed in force couples can create rotation.

## 1.2 Literature Review

### 1.2.1 Reconfigurable RF Circuits

The creation of reconfigurable radio frequency circuits is an effort supported by DARPA being approached by several research groups [4, 5]. The main approach used by these groups is RF field programmable gate arrays (RF-FPGAs) that use switching matrices to select hard-wired components. The architecture of the circuits varies from group to group, but the challenges are shared. Using hard-wired RF components leads to difficulty scaling up, transmission line losses, and system degradation as individual components fail.

#### 1.2.1.1 BAE Systems

BAE Systems has proposed MATRICs (Microwave Array Technology for Reconfigurable Integrated Circuits) in order to create high-performance reconfigurable RF circuits [4]. The device operates from baseband-to-20 GHz, the full range required in most defense applications. It relies on a completely monolithic implementation. The commercial SiGe-on-SOI BiCMOS process precludes the use of most high performance analog components, such as selective RF filters (e.g. surface acoustic wave, quartz, or ceramic filters) [9]. The MATRICs system uses cascades of reconfigurable blocks to achieve the desired performance [4]. While MATRICs provides a compact system without substantial complexity, it does not allow the use of heterogeneous or upgraded RF components that might be able to provide

improved RF performance.

### 1.2.1.2 Northrop Grumman

Northrop Grumman's Electronic Systems (NGES) group is also approaching the RF-FPGA problem [5]. Their transceiver functions from 0.4 Hz to 18 GHz and uses phase change switches to reduce switching losses. Essentially, a web of component banks connected by switches has been proposed. Although the phase change switches reduce switching losses, the addition of components and/or banks leads to longer transmission lines and increased switch counts, both of which contribute to losses in the system. Figure 1.5 demonstrates how a generic switching matrix would behave upon the addition of series components compared to RFactory. RFactory's insertion losses are able to stay low because of the minimal transmission line additions when components are added compared to the switching and transmission line losses added in a generic switching matrix. For NGES, avoiding high insertion losses is a serious concern [5].

### 1.2.2 Micromanipulation

In addition to piezoelectric actuation, MEMS actuation mechanisms that could have been considered for the RFactory system are electro-thermal [10–12], electrostatic [1, 13, 14], distributed air-flow [15], and diamagnetic levitation [16]. Table 1.2 summarizes the translational and rotational capabilities of this previous work.

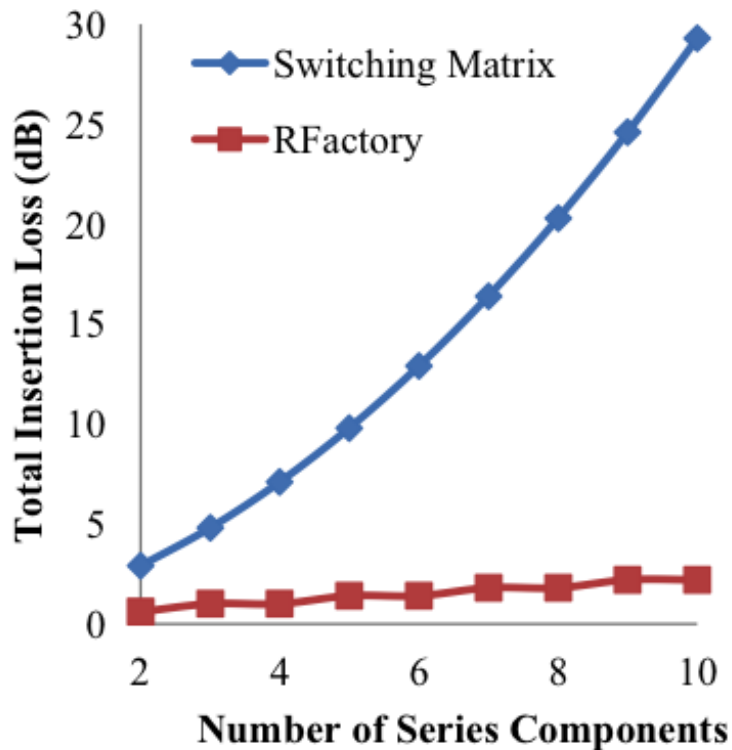


Figure 1.5: The insertion losses for a generic switching matrix become extreme as more series components are added, while RFactory’s insertion losses remain low.

### 1.2.2.1 Electro-thermal Actuators

Polymer thermal bimorphs using differential coefficients of thermal expansion (CTEs) are inherently limited by the low thermal diffusivity of the two layers, making the actuator response slow [17]. The slow response reduces the utility of thermal actuators in RFactory, a system that demands rapid reconfigurability. Suh et al. created MEMS thermal ciliary actuator arrays, shown in Figure 1.6 [10]. These actuators were proposed for use in picosatellites [11] and walking microrobots [12]. The actuators use a CTE mismatch between two polyimide layers. When heated by a re-

Table 1.2: Alternative micromanipulation mechanisms to piezoelectric MEMS.

Actuation Mechanism	Maximum	Maximum
	Translational	Rotational
	Velocity (mm/s)	Speed (RPM)
Electro-thermal [10]	.25	.006
Electrostatic [1]	.2	N/A
Distributed Air-flow [15]	8.3	N/A
Diamagnetic Levitation [16]	375	N/A

sistance heater, the triangular actuators bend out of plane. Suh et al. demonstrated translation of a  $3\text{ mm} \times 3\text{ mm} \times 0.1\text{ mm}$  silicon chip in arbitrary directions as well as rotation using force couples. The maximum translational velocity achieved was 0.25 mm/s and the maximum rotational speed was 0.006 RPM. The power consumption for these actuators was in the  $\text{W}/\text{cm}^2$  range. While the four-actuator configuration is a useful and flexible design, electrothermal actuation has only achieved 0.25 mm/s conveyance velocity, and RFactory requires at least 1 mm/s [10]. Additionally, thermal management could become an issue for the longterm objective of high power RF circuit reconfigurability.

### 1.2.2.2 Electrostatic Actuators

Bohringer et al. used purely electrostatic actuation in their 1996 work on micromanipulation and demonstrated lifting milli-scale glass and paper parts several  $\mu\text{m}$  up and approximately  $100\ \mu\text{m}$  horizontally [18]. This paper reported on the use

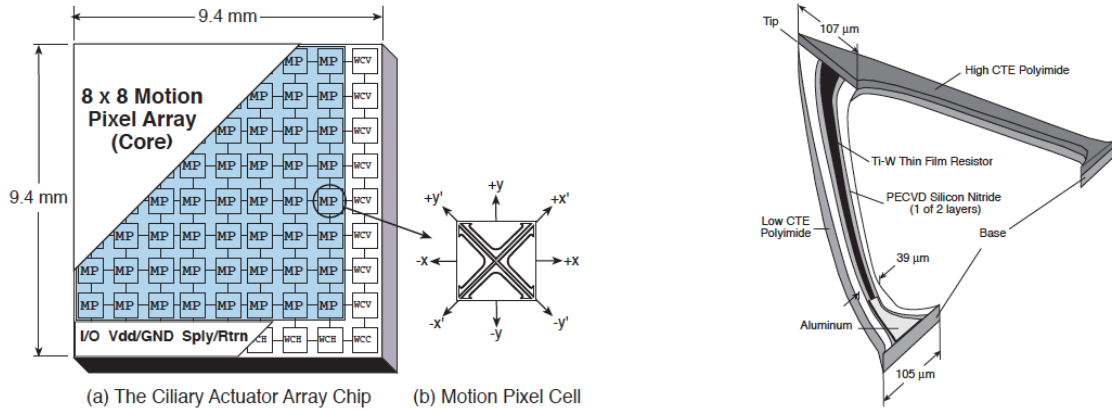


Figure 1.6: Left: a) An actuator surface nearly 10 mm wide was created from a four-actuator unit cell, shown in b) Right: Cross-sectional view of single actuator, showing mismatched coefficients of thermal expansion for the polyimide layers [10].

of torsionally suspended grids of single crystal silicon tips. Each actuator was  $180 \times 240 \mu\text{m}^2$  in size. No speeds were reported for these actuators.

A later paper in 1997 by Bohringer et al. uses both electro-thermal and electrostatic actuation with the actuator shown in Figure 1.7. With these actuators translational velocities of 0.2 mm/s were reported. Rotational results were reported as “several turns” within a 10 minute experiment [1]. The actuator unit cell, at 1.1 mm a side, is larger than some of the parts that RFactory would like to be able to reconfigure, such as discrete capacitors. Additionally, the maximum reported speed is 0.2 mm/s compared to the 1 mm/s RFactory requirement. Also, the electro-thermal and electrostatic combination for actuation requires cooling of the surface to avoid overheating, something that cannot be easily integrated into the RFactory system. The additional weight, volume, and power draw of a cooling system would potentially prevent the bulk piezoelectric actuator from lifting the actuator surface

and exceed the  $5 \text{ cm}^3$  and  $1 \text{ mW}$  volume and power draw objectives of the actuator surface in the RFactory system.

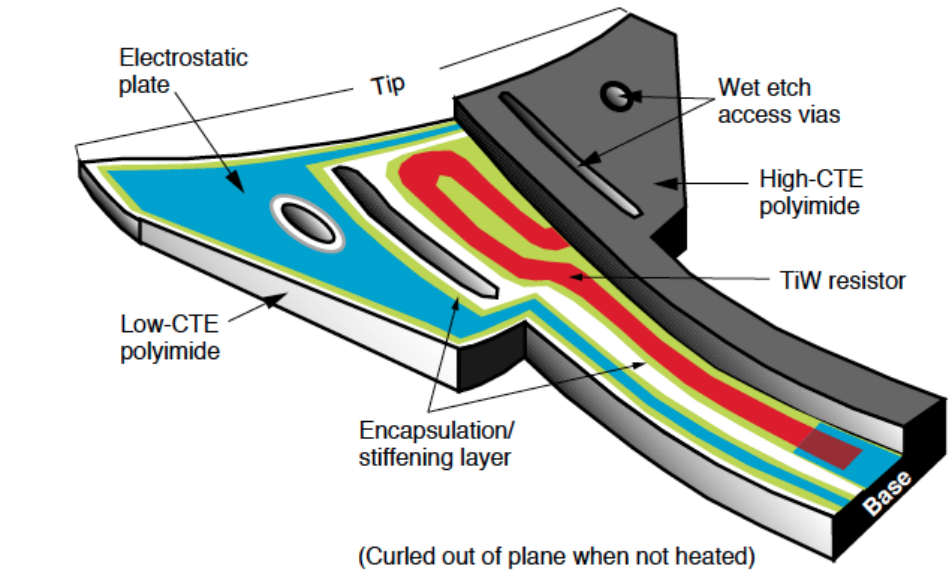


Figure 1.7: Four of these electro-thermal/electrostatic actuators are arrayed orthogonally into a  $1.1 \text{ mm}$  square actuator unit cell in order to create a combined electro-thermal/electrostatic microcilia actuator [19].

### 1.2.2.3 Distributed Air-flow Actuation

Fukuta et al. created a distributed air-flow small-scale manipulation surface [15]. Using a surface interspersed with electrostatically controlled air vents, objects can be levitated and then translated with low friction and higher velocities compared to micromanipulation systems with contact between the surface and the moving component. Fukuta et al. were able to achieve velocities of  $8.3 \text{ mm/s}$ . However, the system requires over  $90 \text{ V}$  to actuate the electrostatic vent controls, much higher than the  $10 \text{ V}$  required for RFactory's piezoelectric actuation. Additionally, it requires a

constant air source, which would greatly increase the overall system size of RFactory. Finally, it has only been demonstrated to manipulate relatively large, light-weight objects like paper [15].

#### 1.2.2.4 Diamagnetic Levitation

Diamagnetic levitation uses the natural repulsion of certain materials, like graphite, by magnetic fields to counteract gravity [20], [21]. Pelrine et al. have demonstrated self-levitating micromanipulators [16]. A printed circuit board (PCB) is covered in graphite, and the manipulators are created by a  $2 \times 2$  grid of small (1 mm diameter) magnets as shown in Figure 1.8. The current running through the traces on the PCB creates a magnetic field that enables levitation and translation. Because the manipulators are levitating, there is no friction and no hysteresis, and velocities of up to 375 mm/s have been demonstrated [16]. In the long-term, electromagnetic interference between the RF components and the magnetic fields are a concern [22].

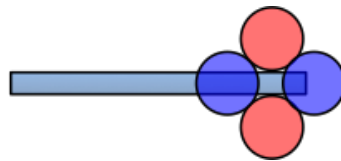


Figure 1.8: This illustration shows an overhead view of the magnets configuration used in diamagnetic micromanipulation with the manipulator arm to the left. South-oriented magnets are shown in red, north-oriented in blue [16].

### 1.2.2.5 Piezoelectric MEMS Actuators

The direct piezoelectric effect is the conversion of mechanical strain to electrical charge seen in certain crystalline materials. The converse piezoelectric effect is the conversion of an electrical field to mechanical strain. This converse effect is useful in actuators and is governed by the tensor equation seen in Equation 1.1. The strain is represented by  $x$ ,  $d$  is the piezoelectric strain coefficient, and  $E$  is the applied field [23].

$$x_{jk} = d_{ijk}E_i \quad (1.1)$$

For piezoelectric MEMS, thin-film piezoelectric materials are often used, and metal layers above and below the piezoelectric layer act as electrodes [23–25]. For the piezoelectric actuation seen in Figure 1.9, the relevant piezoelectric coefficient is  $d_{31}$ . However, in thin films,  $e_{31,f}$ , the effective thin-film piezoelectric stress constant, is a more easily measured quantity that is related to the strain coefficient by the Young’s modulus [23].

Lead zirconate titanate (PZT) is a piezoelectric material that can provide favorable actuation in the  $d_{31}$  direction at the microscale in terms of power draw, electromechanical coupling, and low voltage. Since its development in the 1950s, it has been used in its bulk form in a variety of applications, including ceramic filters. As a thin-film, it can be integrated into microelectromechanical systems (MEMS) for micro- and milli-scale applications. The  $e_{31,f}$  for other common piezoelectric thin films, ZnO and AlN, are  $-0.57 \text{ C/m}^2$  and  $-0.58 \text{ C/m}^2$  respectively. The PZT thin-film  $e_{31,f}$  value is  $-3.0 \text{ C/m}^2$ , nearly 6 times that of the other piezoelectric materials [26].

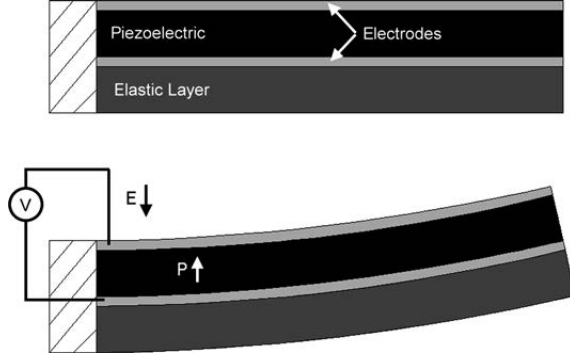


Figure 1.9: For an electric field applied across a piezoelectric thin film located off of the neutral axis of a cantilever, strain is created in the long-axis direction and leads to bending [23].

As an actuator, thin-film PZT can offer large forces and displacements while scaling favorably compared to other thin-film piezoelectrics [8].

### 1.3 Goals and Scope

The goals of the actuator surface characterization and development are defined by the system requirements of RFactory. To obtain electrical contact resistance of  $<1 \Omega$  between the components and the electrical interconnect substrate, the positional errors must be within a certain tolerance. The initial goals of the RFactory system are explained in Table 1.1.

The precision objectives of the RFactory actuator surface are represented by three quantities: on-axis translational error, off-axis translational error, and rotational error. The on-axis translational error represents the difference in on-axis position of a component after some displacement. It is caused by inconsistencies in velocity in the on-axis direction. The off-axis translational position error is the

wandering of the component in the direction perpendicular to the desired direction of motion, called the y-axis. Rotational error describes the discrepancy between the desired orientation and the final orientation of the component chip. Since the majority of characterization has focused on translational actuator surfaces, any change in orientation is unwanted. RFactory eventually intends to operate using integrated capacitive sensors [27], and the main focus of this work is to improve open-loop performance in order to reduce the time spent correcting component position under closed-loop control.

The performance objectives of the actuator surface are translation and rotation speeds. To enable rapid reconfigurability, the translation speed objective is 1 mm/s and the rotation objective is 60 rpm. With these speeds, components can be translated in and out of position with little lag time in RF performance for many applications.

This thesis describes the design, fabrication, and characterization of the actuator surface with the goal of explaining the principle of operation of the MEMS actuator surface and establishing high-quality motion of RF components. Two models, a simple quasi-static model and a multi-physics dynamic model, have been developed. The quasi-static model displays the general trends of motion. The dynamic model illustrates contributing physical phenomena, such as higher order vibrational modes, adhesion, and friction. By focusing experimental tests on one- and two-directional actuator surfaces, the underlying physics were investigated. Three driving signal parameters were varied to study their effect on motion quality: voltage amplitude, waveform, and frequency. The modeling and experimental results led to a clearer

comprehension of the principle of operation of these actuator surfaces, which then led to the development of useful operating conditions capable of producing reliable, precise component motion.

## 1.4 Organization of the Thesis

In chapter 2, the process of designing the actuator arrays and creating appropriate models is explained. The actuator arrays have been designed in order to create two bi-directional translational DOF and one degree of rotational freedom. The modeling work on this project began with a simple quasi-static model, but has been expanded to a full multi-physics model that more completely describes the dynamic phenomena that contribute to the motion of components on the actuator surface.

Next, chapter 3 reports the experimental results of several parametric studies. Waveform, voltage amplitude, and frequency have been varied to obtain ranges of good working conditions for three generations of devices. The experimental results have been compared to the modeling work. Additionally, the design variables of actuator length and width have been varied to create high-performing actuator arrays. The combination of design and actuation parametric variation has led to actuator surfaces capable of performing basic system demonstration of RF reconfiguration.

Finally, the results are analyzed to present a summary of the behavior and optimization capabilities of the RFactory actuator surface. The regions exhibiting the best operating conditions are presented for use in future actuation testing. The

future directions of this research are explained in terms of RFactory objectives and MEMS micromanipulation capabilities.

## Chapter 2: Design and Modeling

### 2.1 Design of the Actuator Surface

The main objective of the actuator surface design is to create reliable, useful motion in up to two bi-directional translational DOF and rotation. Additionally, the actuators must produce consistent translation at  $>1$  mm/s of the component chips resting upon them.

The unit actuator of the RFactory actuator surface is shown in Figure 2.1. The device is a unimorph  $d_{31}$ -mode piezoelectric cantilever actuator. The application of voltage to the parallel plate electrodes induces out-of-plane bending. High aspect ratio metal posts at the free end amplify the actuator deflections in the desired direction of motion. The angular deflection can be seen in Figure 2.2, and the  $\Delta x$  for the post tip can be seen to be significantly larger than the deflection of the cantilever alone. The  $\Delta x_{post}$  is defined in Equation 2.1 where  $\alpha$  is the angular deflection and  $t_{post}$  is the height of the post.

$$\Delta x_{post} = \sin(\alpha)t_{post} \quad (2.1)$$

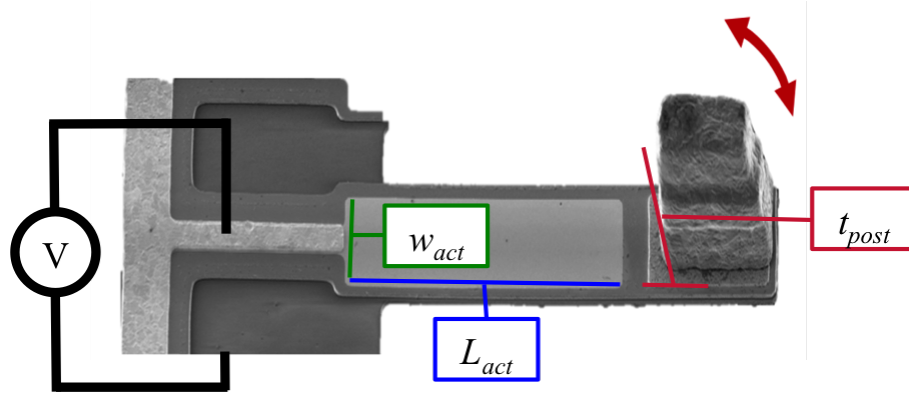


Figure 2.1: This scanning electron micrograph (SEM) was taken at a  $30^\circ$  angle from the vertical and then edited to isolate the unit actuator. The post height ( $t_{post}$ ), actuator length ( $L_{act}$ , and actuator width ( $w_{act}$ ) are illustrated. The red arrow illustrates the out-of-plane bending caused when a voltage is applied.

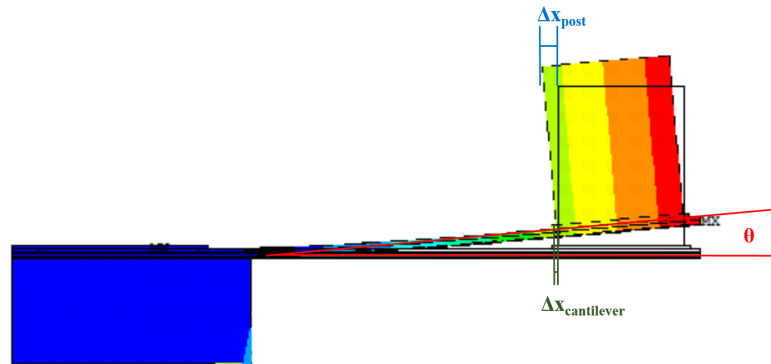


Figure 2.2: The horizontal displacement caused by cantilever angular deflection is exaggerated by the metal post.

### 2.1.1 Quasi-static model

The angular deflection of the cantilever is due to a moment exerted on the cantilever by the piezoelectric actuator, located at a distance  $h_{PZT}$  from the neutral axis. Figure 2.3 shows the moment acting on the actuator. This moment depends on

the voltage applied across the piezoelectric layer. Equation 2.2 shows the moment's dependence on the piezoelectric strain constant  $e_{31}$ , voltage  $V$ , actuator width  $w_{act}$  and distance between PZT and neutral axis  $h_{PZT}$ .

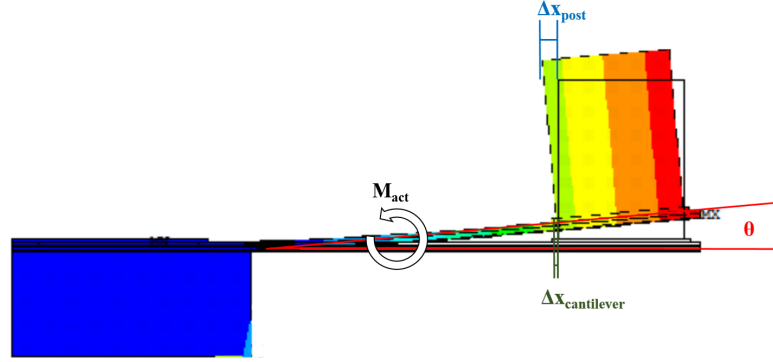


Figure 2.3: The angular deflection of the actuator depends on the moment caused by the application of voltage across the piezoelectric layer.

$$M_{act} = e_{31} V w_{act} h_{PZT} \quad (2.2)$$

The angular deflection,  $\alpha$ , can be calculated from the actuator moment, the piezoelectric stress constant  $e_{31}$ , the actuator length, the Young's modulus, and the moment of inertia of the cantilever, idealized to a beam. Equation 2.3 shows the relation. Because  $I = wh^3/12$ , the angular deflection is also affected by the actuator width. The piezoelectric stress constant was measured previously [8].

$$\alpha = \frac{M_{act} L_{act}}{EI_c} \quad (2.3)$$

From the static post tip deflection calculated in Equation 2.1, a quasi-static step size for a cycle of actuation is calculated. This assumes that the chip resting

on the actuator obtains the full forward horizontal displacement of the actuator at maximum voltage. To obtain a chip velocity, the step size is multiplied by the frequency of actuation, as shown in Equation 2.4. The predicted quasi-static response to variation of actuator ramping speed, voltage amplitude, and frequency are discussed in Chapter 3 with experimental results. In addition, the expected effect of actuator length and width has been calculated, as shown in Figure 2.4.

$$\dot{x}_{post} = \Delta x_{post} f_{act} \quad (2.4)$$

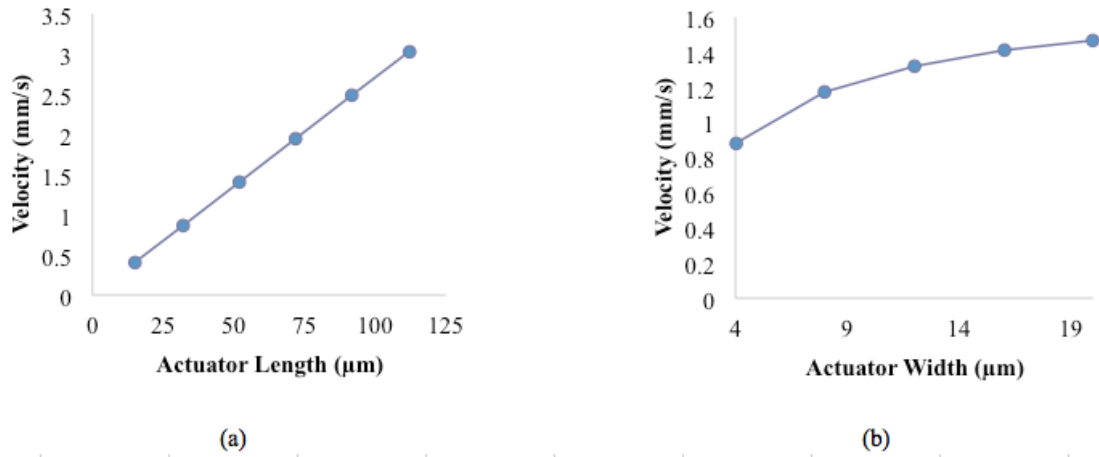


Figure 2.4: The quasi-static model predicts the length and width dependence for an experiment with  $t_{post}=30 \mu\text{m}$ , voltage=8 V, and frequency=500 Hz. (a) Increasing actuator length is expected to lead to proportionally increased velocity. Actuator width is 16  $\mu\text{m}$ . (b) As the actuator width increases, the additional velocity predicted becomes less significant. Actuator length is 52  $\mu\text{m}$ .

### 2.1.2 Multi-physics Dynamic Model

The quasi-static model is a useful simplification of the actuator surface conveyance, but it does not reflect the physical reality of the system. The quasi-static model ignores the interaction of the component and actuator as the actuator returns to its initial position. It also assumes that the transfer of motion between the actuator and component is perfect. To capture the physics of operation of the system, a multi-physics dynamic model was designed. It takes into account the component-actuator interaction throughout the entire cycle of actuation as well as considering microscale phenomena like contact and air damping.

The process used to model the actuator behavior was adapted from the dynamics of micro-switches previously reported by Pulskamp et al. [31]. The micro-switch model used modal superposition to obtain the time domain dynamics of the switches. To summarize the actuator surface dynamic model development, first the modal behavior of an actuator was studied as well as an actuator with constrained component (actuator-component) system. Both cases are shown in Figure 2.5. Then, other physical phenomena, such as contact state and friction modulated adhesion, were incorporated into the model by my collaborator, Mr. Jeffrey Pulskamp. Table 2.1 summarizes the key physical phenomena incorporated into the model. The dynamic model is compared to the experimental results in Chapter 3. The following discussion incorporates my contribution to the dynamic model – the modal analysis.

Using ANSYS finite elements analysis (FEA) software, the resonant frequen-

Table 2.1: The dynamic model includes the following elements.

Key Elements of the Multi-Physics Dynamic Model
Dynamics of Actuator
Projectile Motion
Contact State
Adhesion
Frictional Slip in X Direction
Multiple Modes of Actuators
Mode Transitions (Contact and Freefall)
Air Damping

cies and mode shapes of the actuator alone and the actuator-component system were calculated. The model used SOLID92 element types to create a geometry that included an abridged Si chip 20  $\mu\text{m}$  thick, an alternating oxide/nitride/oxide layer with thicknesses of 0.1/0.2/0.7  $\mu\text{m}$  respectively, a bottom electrode layer of 0.125  $\mu\text{m}$  of platinum, a 0.52  $\mu\text{m}$  of PZT, a 0.05  $\mu\text{m}$  of top platinum electrode, a 0.77  $\mu\text{m}$  thick gold metal traces and post anchor, and a 30  $\mu\text{m}$  tall copper post. The geometry and layers are slightly simplified from the actual fabrication. For example, the 0.125  $\mu\text{m}$   $\text{TiO}_2/\text{Pt}$  bottom electrode has been simplified to a 0.125  $\mu\text{m}$  Pt layer. Despite the need for  $\text{TiO}_2$  in fabrication to reduce Pt diffusion, it is not structurally significant. Other simplifications, such as idealizing the undercut geometry and reducing the chip size (increasing density to account for the volume change), were performed in order to reduce the processing time necessary to mesh and solve the

system. The geometry of the actuator model and the actuator-component system can be seen in Figure 2.5.

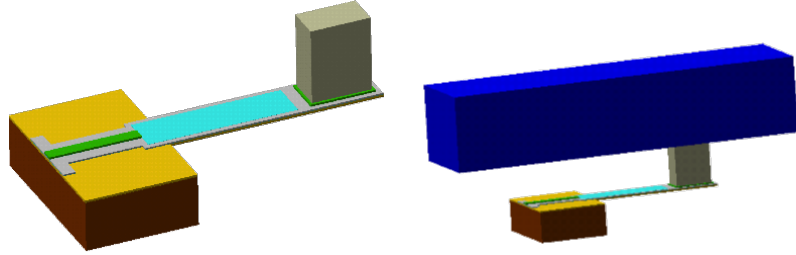


Figure 2.5: Left: The single actuator model in ANSYS. Right: The representative geometry of a single actuator in contact with a chip. Colors indicate different materials.

Two analyses were performed: one with the actuator on its own, and one with the actuator in contact with a representative portion of a silicon chip. In both models, the silicon wafer was clamped in X, Y, and Z. For the actuator-component system, the two post corners furthest from the anchor were coupled in X, Y, and Z with the two coincident points on the component chip in the initial position. Additionally, the four top corners of the component chip were coupled in Z, in order to suppress bulk modes in the chip. A rough mesh of  $25\ \mu\text{m}$  element length was set for the chip,  $10\ \mu\text{m}$  for the silicon wafer, and  $4\ \mu\text{m}$  for the cantilever and post.

A modal analysis using the Block-Lanczos solver was performed for each case [32]. The first twenty modes were solved for and expanded in order to capture some higher-order modes without adding excessive processing time. The modes were mass-normalized in order to create the mode shapes. In post-processing, the modes were plotted with their deformed shape and a contour of the z-displacement.

In order to obtain the nodal displacements of the copper post, another ANSYS code was used to extract the z-displacements from each mode. From the first 20 modes, only the modes that demonstrated a non-zero piezoelectric modal force, i.e. the actuator was displacing the chip, were chosen. Some modes did not affect the chip and others were bulk modes within the chip, unrelated to the piezoelectric actuation. An example of a significant mode can be seen in Figure 2.6, while a mode that was neglected is shown in Figure 2.7.

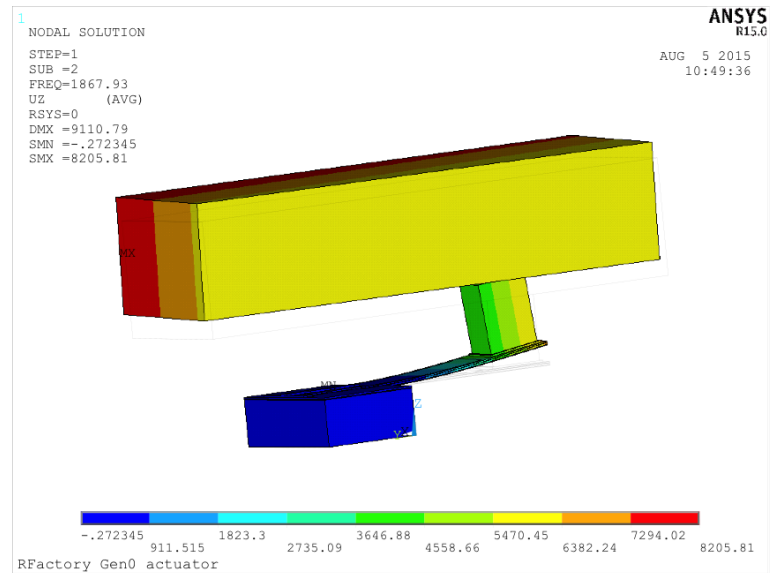


Figure 2.6: The z-displacement contour plot of the deformed shape of the actuator-component system shows that the actuator is exerting force on the component chip.

The significant modal behavior is combined with contact transition behavior and other micro-scale phenomena to yield the final dynamic model in the time domain. The modal forces and time domain dynamics were calculated in MATLAB for the modes identified in FEA. Then the results were superimposed to obtain the time domain dynamic behavior of the actuator. The predicted actuator motion

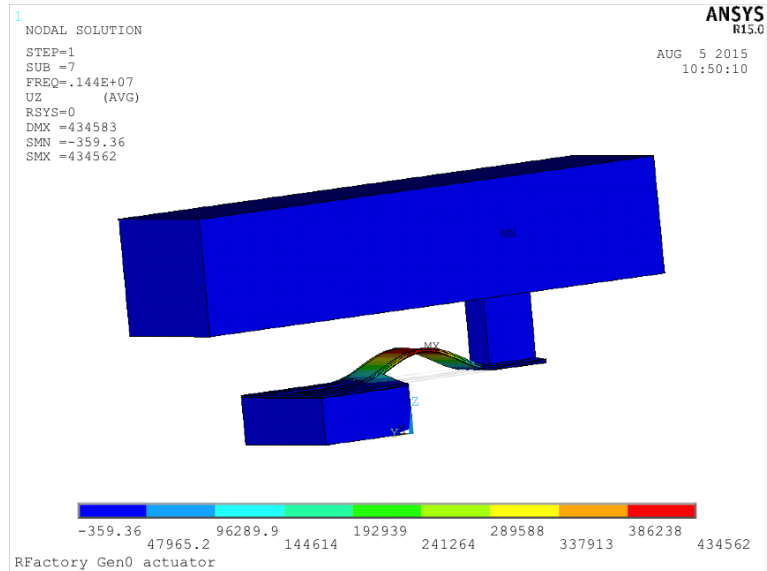


Figure 2.7: In this mode, the actuator post is not displaced, so the mode would not contribute to component motion and it has been left out of the dynamic model.

was then applied to the component. The model predicts that the component varies between projectile motion and coupled motion with the actuators, which creates a "hopping" mechanism of component motion. The ringing of the actuator, shown in Figure 2.8, particularly in the down phase of a leading edge ramp wave, causes more complex contact/non-contact transitions. Not only does the component transition between projectile motion and coupled motion, but the actuator transitions between different modal behavior when in and out of contact with the component. Added to these dynamics are contact behavior for friction, adhesion, and air damping.

Figure 2.9 demonstrates the importance of the development of the dynamic model. While the quasi-static model agrees trend-wise with the experimental results, significant deviation occurs above 800 Hz. The agreement of the dynamic model, especially from 200 Hz to 500 Hz shows that the undulating quality of the

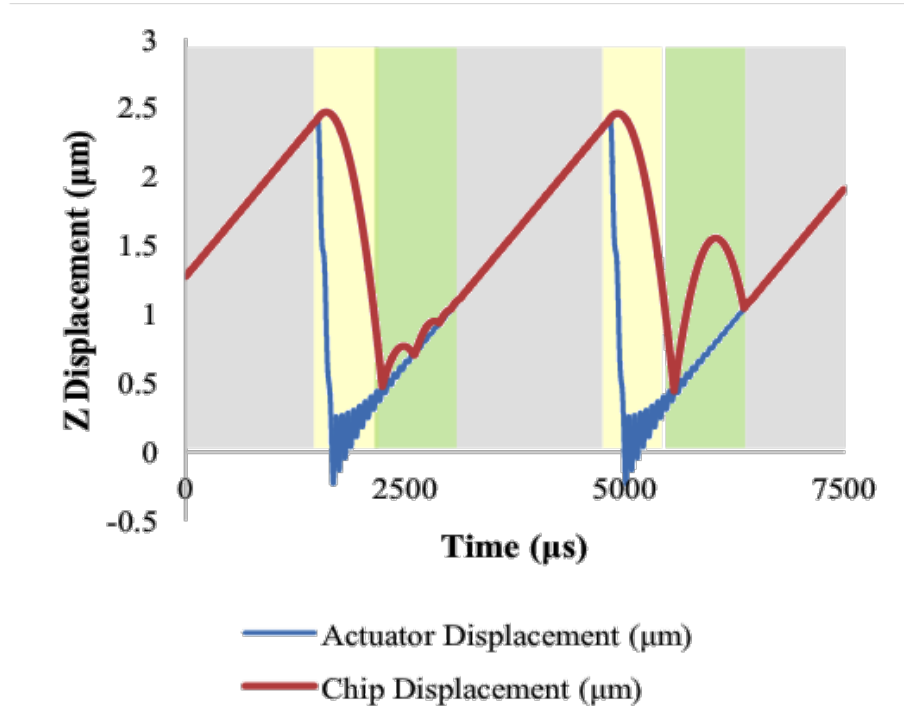


Figure 2.8: The dynamic model predicts that the cantilever experiences significant ringing. This interacts with the chip’s motion as it transitions between actuator-coupled motion and projectile motion. The gray shading illustrated motion where the actuator and chip are coupled. The yellow region is projectile motion and the green region highlights the ringing interaction caused by the cantilever dynamics.

experimental data can be observed and accounted for in the dynamic model. The dynamic model captures the physics of operation behind the complex motion of a component on the actuator array.

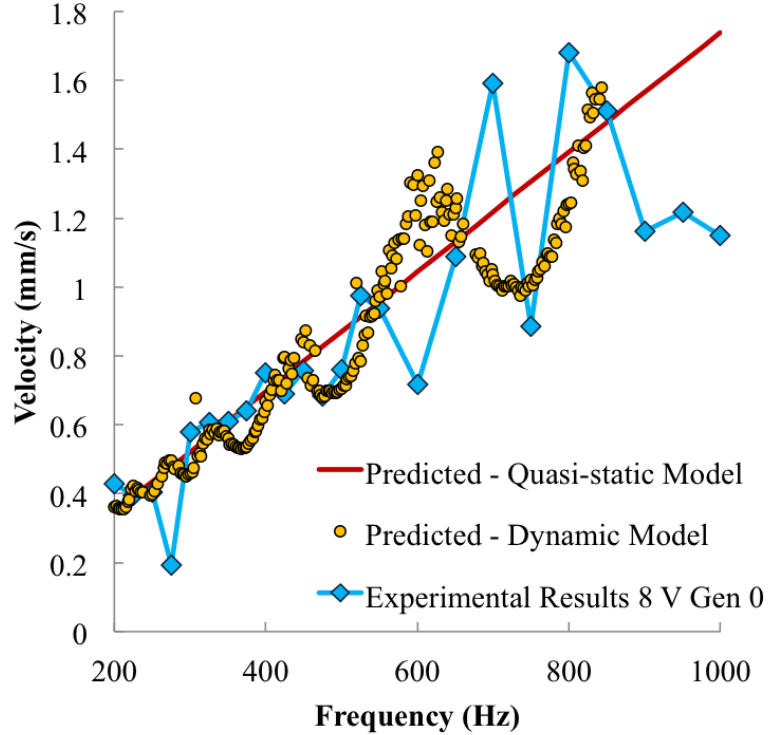


Figure 2.9: This plot demonstrates the improvement of the modeling from quasi-static to dynamic models. The quasi-static agrees trend-wise, but the dynamic model demonstrates qualitative agreement, especially between 200 Hz and 500 Hz.

### 2.1.3 Array configurations

In order to address directional flexibility, actuator arrays have been designed in four primary configurations, shown in Figure 2.10. The basic configuration uses rows of identically aligned actuators. These arrays are capable of one degree of translational freedom, called 1D or +X. Sets of opposing actuator rows can induce bi-directional motion (2D or +/-X). Two bi-directional translational DOF (+/-XY) can be achieved by a unit cell of orthogonally arranged actuators. Rotation is achieved by utilizing rows of unit actuators arranged as force couples.

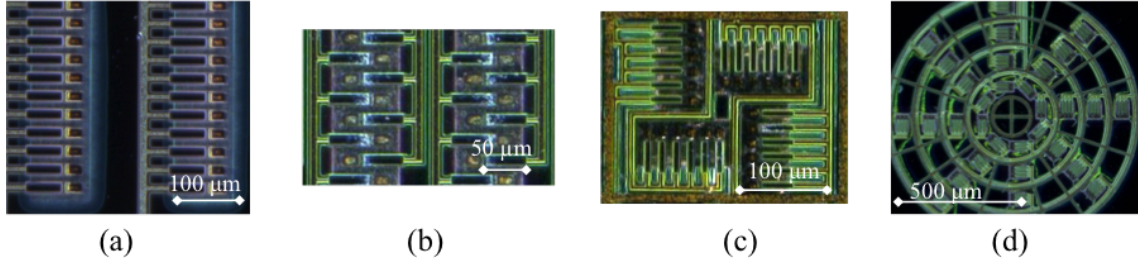


Figure 2.10: (a): One directional actuator array oriented to drive chips to the left. (b): 2D or +/-X actuator array shown oriented for left/right motion. (c): Two bi-directional translational DOF can be actuated by this array, also called +/-XY. (d): Force couples create rotation.

#### 2.1.4 Fabrication

The actuator surface capitalizes on the PZT multi-layer-metal fabrication process developed at the US Army Research Laboratory to create active cantilevers integrated with tall ( $30\ \mu\text{m}$ ) posts made of metal [28]. The fabrication process, performed by the PiezoMEMS and Microsystems Power Components teams' process engineers and technicians, follows the steps detailed in Figure 2.11. A multi-layer composite of  $\text{SiO}_2$  and  $\text{Si}_3\text{N}_4$  with a thickness of approximately  $1\ \mu\text{m}$  is deposited on a silicon wafer using plasma enhanced chemical vapor deposition, followed by a  $\text{TiO}_2/\text{Pt}$  electrode, which also acts as a template for PZT growth. Using a chemical solution process,  $0.5\ \mu\text{m}$  of PZT with a Zr/Ti ratio of 52/48 is deposited. Above this, another platinum electrode is deposited. Then these layers are patterned and a Ti/Pt/Au layer is deposited and patterned. Photoresist is used as a mold for electroplated copper or gold. The photoresist mold is then removed and a  $\text{XeF}_2$  etch

releases the cantilevers [29]. The finished devices are shown in Figure 2.12. The actuator lengths, widths, and post material were varied across the device generations, which are summarized in Table 2.2.

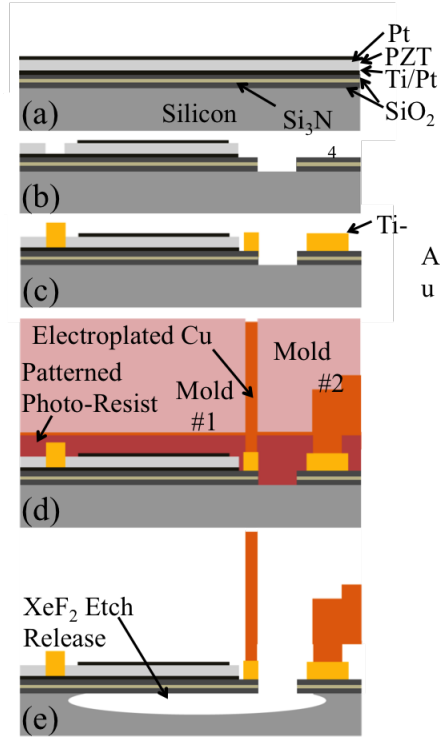


Figure 2.11: This abridged process sequence demonstrates the steps necessary to create the PZT-enabled actuator surface.

Table 2.2: Summary of the device generations for the RFactory actuator surface.

Device Generation	Length(s) ( $\mu\text{m}$ )	Width(s) ( $\mu\text{m}$ )	Post Material
0	52	16	Cu
1	32, 52, 72	8	Cu
2	92	16	Au
3	15, 32, 52, 72, 92, 112	8, 16	Cu

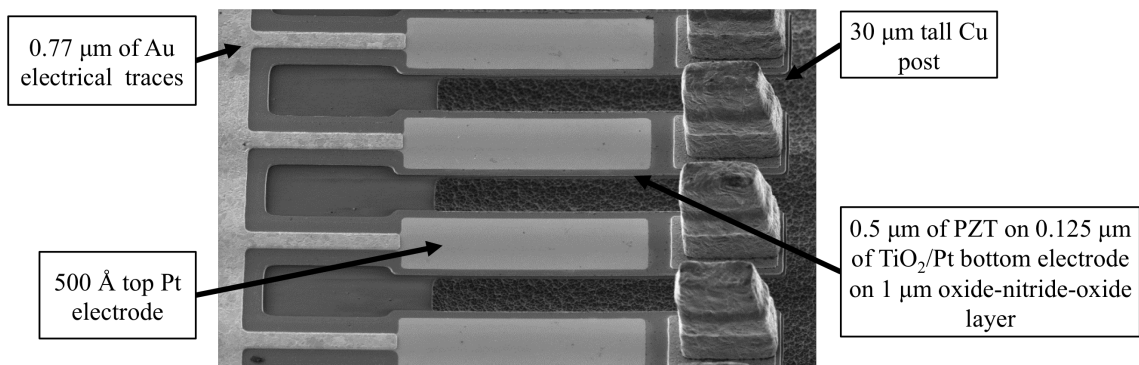


Figure 2.12: This scanning electron micrograph shows the elastic layer and the tall copper posts of a first generation one-directional actuator array.

## Chapter 3: Testing and Characterization

Characterization efforts focused on observing motion quality by manipulating the waveform, voltage, and frequency of the driving signal. Additionally, the impact of actuator length and width was studied.

### 3.1 Metrics

Two primary metrics were selected to evaluate motion quality: distance interval error (DIE) jitter (analogous to timing interval error (TIE) jitter in precision oscillators or clocks) and velocity in the desired direction of motion, denoted as on-axis or X velocity. While TIE jitter quantifies the timing discrepancy between actual and expected signals, DIE jitter was developed to quantify the motional noise of expected position and orientation to actual position and rotation as shown in Figure 3.1. This noise has then been normalized to project objectives so as to be unitless and a jitter value of 1 means objectives have been met. Tests where the chip moves with a constant velocity and little off-axis wandering or rotation have a very low DIE jitter ( $<1$ ), but tests with stalls, wandering, and rotation have a high DIE jitter ( $>10$ ). Using on-axis velocity and DIE jitter captures the speed and precision of the component motion in just two convenient metrics.

Several additional metrics were evaluated in order to calculate on-axis velocity and DIE jitter from experimental data. “Instantaneous” on-axis velocity was calculated between frames of video and then averaged per experiment to give the average on-axis velocities reported later. Off-axis velocity and angular velocity were also calculated. Instantaneous on-axis ( $J_x$ ), off-axis ( $J_y$ ), and angular jitter ( $J_{theta}$ ) were calculated using Equations 3.1, 3.2, and 3.3 respectively.  $x$ ,  $y$ , and  $\theta$  represent on-axis and off-axis position and orientation, respectively. The average on-axis velocity for a given experiment is represented by  $\bar{v}$ . Translational jitter was calculated using Equation 3.4.

Overall instantaneous DIE jitter (normalized to the project objectives) was calculated using Equation 3.5. The total on-axis displacement is represented by  $\Delta x$ , which varies based on the frames of video processed, the length of the actuator array, and the time that the array was actuated. The weighting of the individual jitter components comes from the objectives for component motion seen in Table 1.1. An overall DIE jitter value of 1 indicates that mean square error for all of the objectives has been met.

$$J_x = x - (x_0 + \bar{v}t) \quad (3.1)$$

$$J_y = y - y_0 \quad (3.2)$$

$$J_\theta = \theta - \theta_0 \quad (3.3)$$

$$J_t = \sqrt{J_x^2 + J_y^2} \quad (3.4)$$

$$J_{Overall} = \sqrt{\frac{\left(\frac{5mm \times J_y}{200\mu m \times \Delta x}\right)^2 + \left(\frac{5mm \times J_x}{100\mu m \times \Delta x}\right)^2 + \left(\frac{5mm \times J_\theta}{10^\circ \times \Delta x}\right)^2}{3}} \quad (3.5)$$

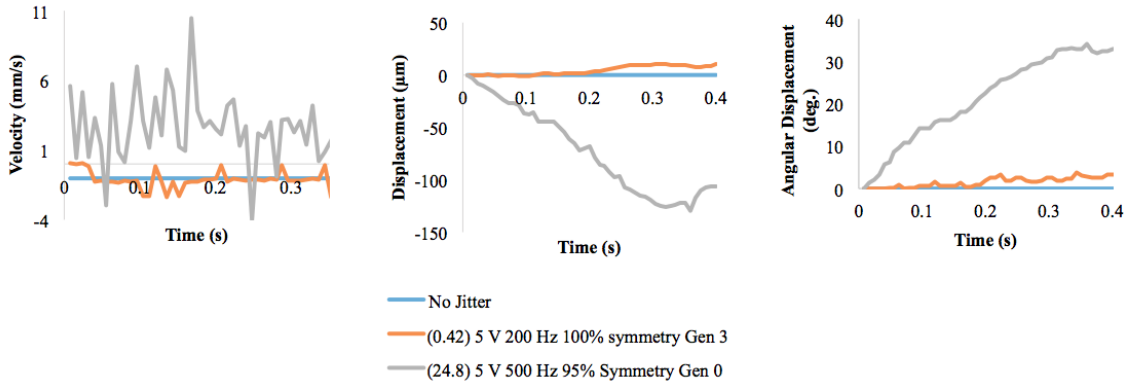


Figure 3.1: No jitter, jitter  $<1$ , and jitter  $>20$  are compared in terms of on-axis velocity, off-axis displacement, and angular displacement. The ideal performance would have a constant on-axis velocity and zero off-axis or angular displacement.

### 3.2 Experimental Procedure

The plots in Chapter 3 represent data taken from device tests from four design generations. Each colored line represents one set of experiments. Most experimental sets used three data points per operating condition, with the exception of four data points for all Gen. 3 devices. Each data point represents an average of the experiments performed at identical operating conditions. The per-experiment averages of on-axis velocity or DIE jitter have been averaged together to find the mean and standard deviation between experiments. The metrics have been plotted with error bars representing one standard deviation between experiments at the same operating conditions. Plots without error bars had one data point per operating condition, which can be seen in some Gen. 0 devices. The number of frames varies from 50 to 5000. Gen. 0 and Gen. 1 tests averaged 50 frames processed, due to the limitations

of the video processing software. After commercial motion tracking software was acquired, thousands of frames were captured and averaged for each experiment in Gens. 2 and 3.

### 3.2.1 Measuring Experimental Data

Using a Keyence VW-9000 series high-speed microscope, seen in Figure 3.2, the motion of a component chip on the actuator surface was measured. The main components carried on the actuator surface are  $500\ \mu\text{m} \times 500\ \mu\text{m} \times 500\ \mu\text{m}$  silicon chips and Qorvo Tri-Quint surface acoustic wave (SAW)  $1.2\ \text{mm} \times 1.4\ \text{mm}$  RF filters. The surface of the silicon chip in contact with the actuator surface has varied over the course of experimentation, with earlier tests using one of six cut surfaces of the silicon wafer and later tests using exclusively the polished side of the silicon wafer. Later tests ensured consistent orientation by using a vacuum-picking system. Earlier tests used tweezers for placement and were less controlled in releasing the component chip onto the actuator surface.

Initially, a MATLAB code was developed to detect the position and orientation of the chip on the actuator surface using an algorithm that finds an area of higher reflectivity and then finds the orientation at which an overlaid square is most aligned. The frame rate for the videos processed using this code was 15 frames per second (fps). This code, used for Gen. 0, was unable to process more than 80 frames. In order to observe the maximum capabilities of the early devices, an average of 50 frames of the most consistent motion was processed. Processing only the

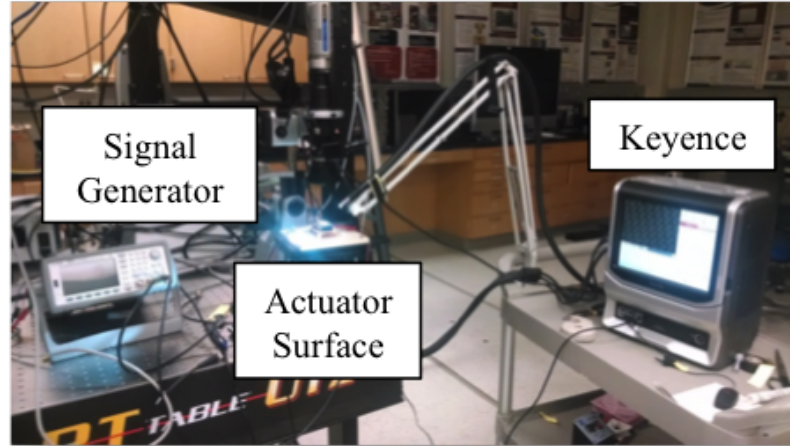


Figure 3.2: A Keyence VW-9000 high-speed microscope was used to examine the component motion on the actuator surface.

most consistent motion also avoided rotational error introduced by the MATLAB algorithm during stalls, which Gen. 0 parts suffered heavily from.

For several experimental sets in Gen. 0 and for all of Gen. 1 testing, another MATLAB code was developed to use the texture characteristics of unpolished silicon to detect the location and orientation of the chip more efficiently using 125 fps video. The output of this MATLAB code can be seen in Figure 3.3 and the code can be found in Appendix A. Later 125 fps videos were processed using the Keyence Motion Analyzer software that was acquired after Gen. 1 processing. The corners of the component chips were tracked and then the centroid and orientation were extracted.

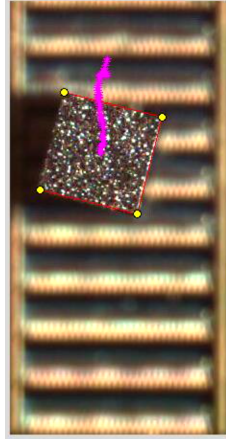


Figure 3.3: The output from the MATLAB motion tracking code shows the detected centroid per frame in magenta and the detected outline in red with yellow corners overlaid over the video frame.

### 3.2.2 Applied Signals

The signal applied to the actuator surface was varied to determine the effect of waveform and waveform symmetry, applied voltage, frequency, and actuator length and width on the chip motion. The various test cases are summarized in Table 3.1. Note that not all conditions were tested on all device generations. Early tests of waveform, for example, showed that ramp waves provided relatively low DIE jitter and were therefore used in all future trials.

Table 3.1: Summary of the signals applied to the devices. It is organized into categories of tests (navy blue), then the type of test within the category (light green), and finally the parameters of the test (light blue).

Waveform
Waveforms with varied frequency at 5 V peak voltage
Sine
Square (50% duty cycle)
Leading edge ramp wave (100% symmetry ramp)
Variation of symmetry (% of period used to ramp up to peak voltage)
0 to 100% symmetry
5 V peak voltage
250, 500, and 750 Hz
Voltage
Voltage amplitude from 2 V to 10 V
500 Hz 100% symmetry on Gen. 2c
750 Hz 90% symmetry on Gen. 0
Frequency
Drive frequency from 100 Hz to 1000 Hz
8 V 100% symmetry on Gen. 0
10 V 100% symmetry on Gen. 0
5 V 100% symmetry on Gen. 0
5 V 100% symmetry on Gen. 2c

Table 3.2: Summary of the design variables tested for the actuator surface. It is organized into categories of tests (navy blue), then the type of test within the category (light green), and finally the parameters of the test (light blue).

<b>Length</b>
Unidirectional
15 $\mu\text{m}$ , 32 $\mu\text{m}$ , 52 $\mu\text{m}$
Bidirectional
32 $\mu\text{m}$ , 52 $\mu\text{m}$ , 72 $\mu\text{m}$ , 92 $\mu\text{m}$ , 112 $\mu\text{m}$
<b>Width</b>
8 $\mu\text{m}$
15 $\mu\text{m}$ , 32 $\mu\text{m}$ , 52 $\mu\text{m}$ , 92 $\mu\text{m}$
16 $\mu\text{m}$
15 $\mu\text{m}$ , 32 $\mu\text{m}$ , 52 $\mu\text{m}$ , 72 $\mu\text{m}$ , 112 $\mu\text{m}$

### 3.3 Waveform Results

The choice of drive waveform has a significant effect on the component motion because the waveform defines the behavior of each cycle of out-of-plane piezoelectric bending. The majority of testing was performed with ramp waveforms at 100% symmetry. This waveform was initially chosen because the original hypothesized principle of operation was based on a stick-slip condition. A leading edge ramp signal would provide a horizontal displacement and then a nearly instantaneous step down would allow the actuator posts to slip, resulting in an incremental displacement in the desired direction. This initial hypothesis has been shown to be insufficient to explain the observed motion.

Testing other waveforms was important to validate continued use of the ramp signal after the model indicated that the principle of operation was based on “hopping” than stick-slip. The velocity results of the waveform variation testing can be seen in Figure 3.4. Square waves were capable of producing displacements at much lower frequencies, likely due to the high launch velocities achieved by the actuators during the step up phase of the wave. Sine waves, on the other hand, managed very minimal displacements until approximately 500 Hz. The 5 V 100% symmetry tests on the Gen. 0 and Gen. 2c devices show similar trends, increasing until approximately 800 Hz and then decreasing. The 5 V ramp wave on the Gen. 2c device shows comparable velocity performance to the sine wave up until around 750 Hz.

The highest DIE jitter was seen in the low frequency sine waves, shown in Figure 3.5. This was mostly due to the negligible displacements experienced at

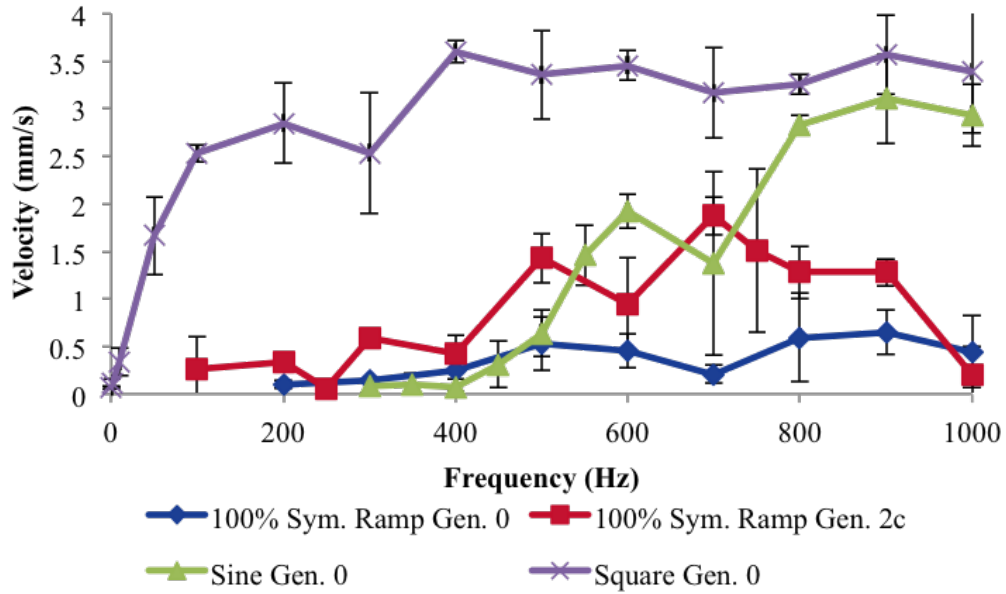


Figure 3.4: The on-axis velocity response of ramp, sine, and square wave driving signals shows that the highest velocities are achieved by square waves. Sine and ramp waves show improved speeds above 500 Hz. All devices used in waveform testing are  $52 \mu\text{m}$  long and  $16 \mu\text{m}$  wide.

those frequencies. With jitter based upon deviation after a 5 mm displacement, low displacements can lead to very high jitter values. The most reliable waveforms appear to be ramp and square waves. The ramp waveforms produce the best jitter values between 500 Hz and 900 Hz, and the square waves produce jitter values of 10 or below. However, the rotation of the square wave was observed to be significant during experimentation. The highlighted region under  $10^\circ$  of the angular jitter in Figure 3.6 shows that for all but one point, the angular jitter of the square wave does not achieve the project objective for angular error. Due to the rotation of the square wave, the ramp waveform was chosen as the preferred drive waveform.

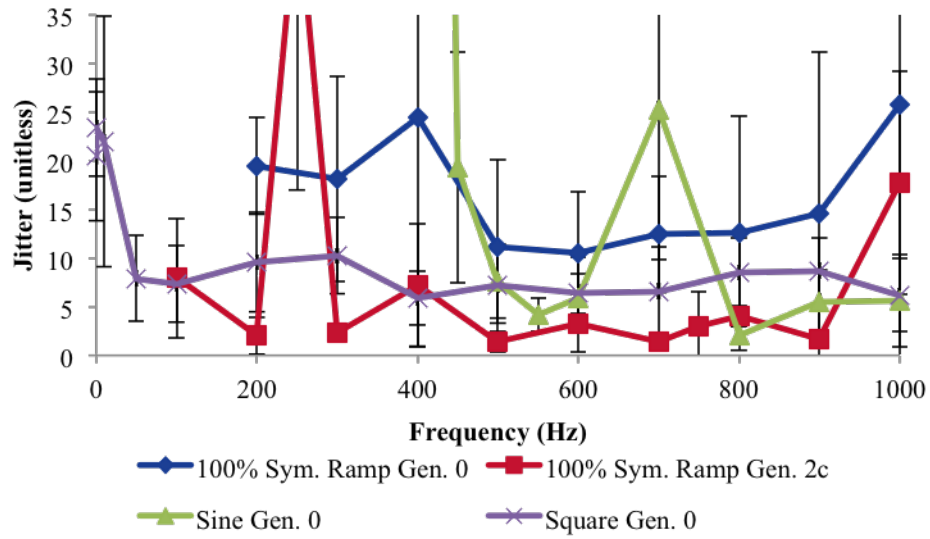


Figure 3.5: An overview of the jitter performance of the various waveforms shows very high and variable jitter values for the sine wave compared to the other waveforms, especially below 500 Hz.

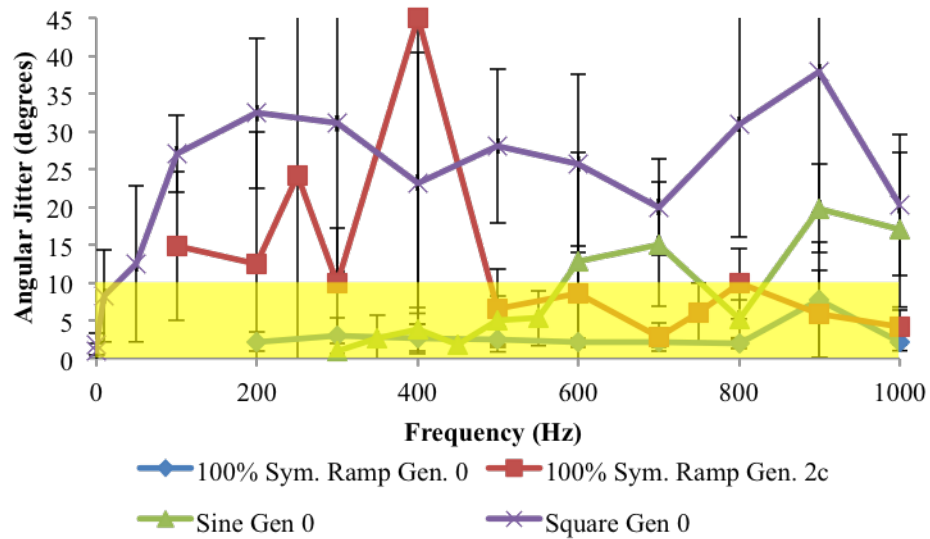


Figure 3.6: The angular jitter values of square waves are above the goal levels for angular error, while the ramp waves meet project objectives above 500 Hz.

Further waveform testing examined the impact of symmetry of ramp waves on operation. Symmetry is the percent of the period used to ramp up the signal to peak voltage, so 0% symmetry is a trailing edge ramp wave while 100% symmetry is a leading edge ramp wave. Symmetries from 0% to 100% were tested at 5 V on two devices and at 250 Hz, 500 Hz, and 750 Hz. The on-axis velocity response seen in Figure 3.7 shows poor velocity performance for 250 Hz and 500 Hz between 40% and 80%. The 750 Hz test is the most consistent across symmetry values. In terms of velocity, the best response is at low symmetries, followed by high symmetries, with poor performance near 50% symmetry.

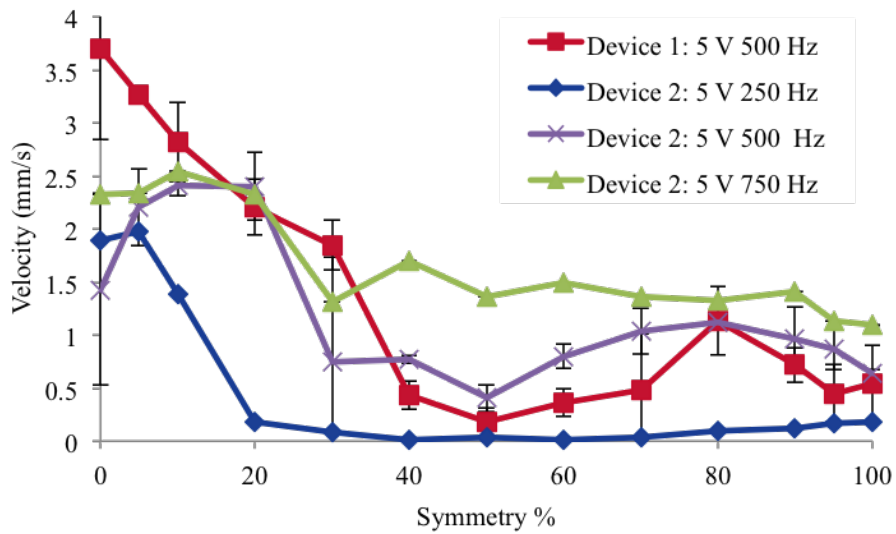


Figure 3.7: The on-axis velocity response generally decreases as ramp waveform symmetry increases.

In terms of overall DIE jitter, Figure 3.8 shows that again, 250 Hz had the worst performance across all four tests, and the best jitter performance across all four operating frequencies is at 100% symmetry. Accuracy is prioritized over speed for

RFactory because the electrical contact performance of the compliant contacts in the interconnect substrate depends on how accurately the component has been placed. Based on this priority, 100% symmetry is the most useful ramp wave symmetry for RFactory.

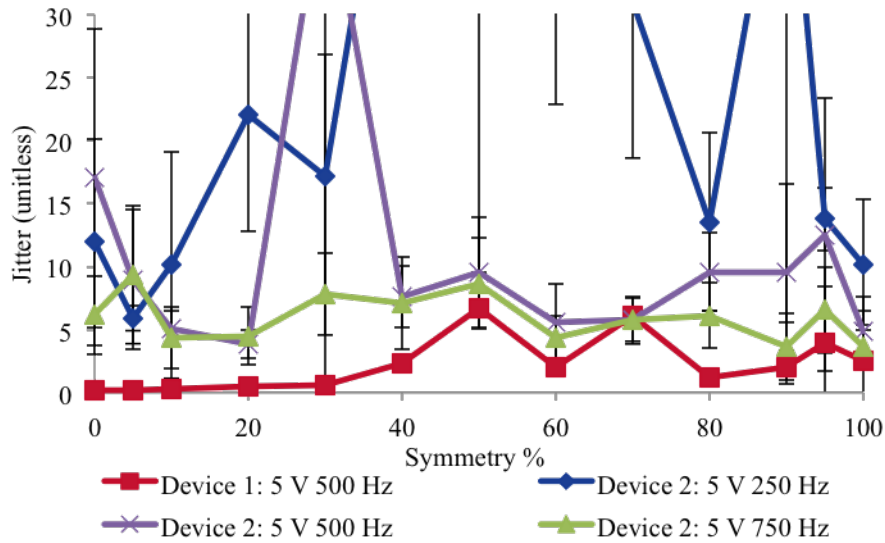


Figure 3.8: The 250 Hz experimental test shows the highest jitter values across the range of symmetries.

The quasi-static model predicts low symmetry response poorly, but matches fairly well close to 50% symmetry as seen in Figure 3.9. The poor low-symmetry agreement is likely due to the dynamic effects that are predicted in the dynamic model for high actuator velocities. Lowering symmetry at a given voltage and frequency increases peak actuator accelerations, which leads to complex dynamics not accounted for in the quasi-static model, such as component-actuator interactions during ringing.

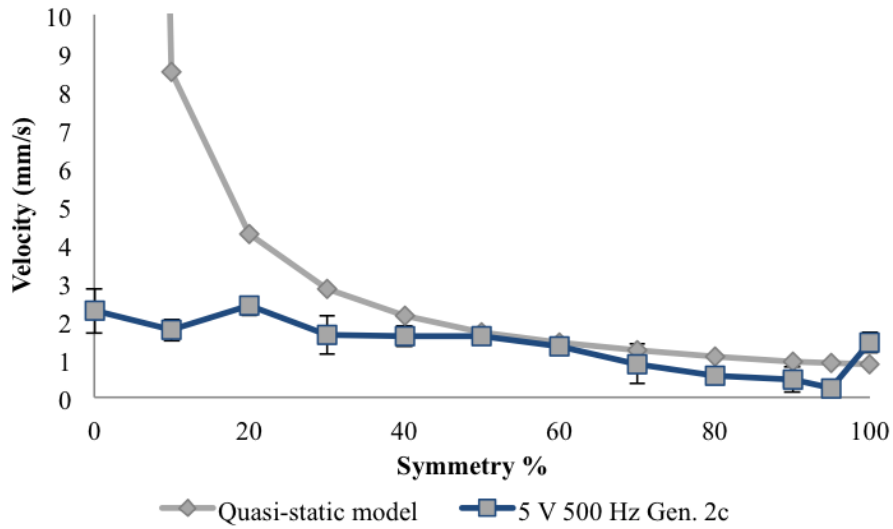


Figure 3.9: The quasi-static model predicts the velocity response to symmetry poorly except in the region near 50% symmetry.

### 3.4 Voltage Amplitude Results

The drive amplitude was varied from 2 V to 10 V at 500 Hz at 100% symmetry and 750 Hz at 90% symmetry. Preferential regions of operation with velocities over 1 mm/s are found above 4 V, especially between 5 and 6 V and at 10 V, as shown in Figure 3.10. While the actuator surface is being driven at an insufficient voltage to overcome adjacent posts, rapid bi-directional rotation of the component is observed, leading to high jitter levels, shown in 3.11.

The voltage amplitude variation study offers useful regions of operation for high speeds and low jitter values. In order to create consistent motion, the voltage must be higher than 4 V. To keep jitter values low, the voltage amplitude should be kept between 4.5 and 8 V.

The quasi-static model shown in Figure 3.12 predicts that the on-axis velocity will increase with voltage amplitude, but the experimental results show that below 4 volts for 500 Hz and 100% ramp wave symmetry, the deflection is insufficient for significant motion.

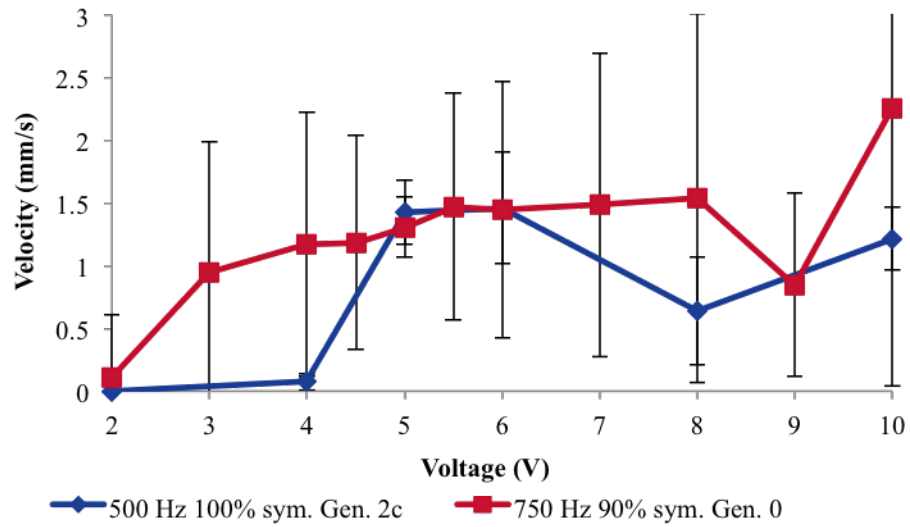


Figure 3.10: The on-axis velocity response due to voltage amplitude shows the best performance above 4 V.

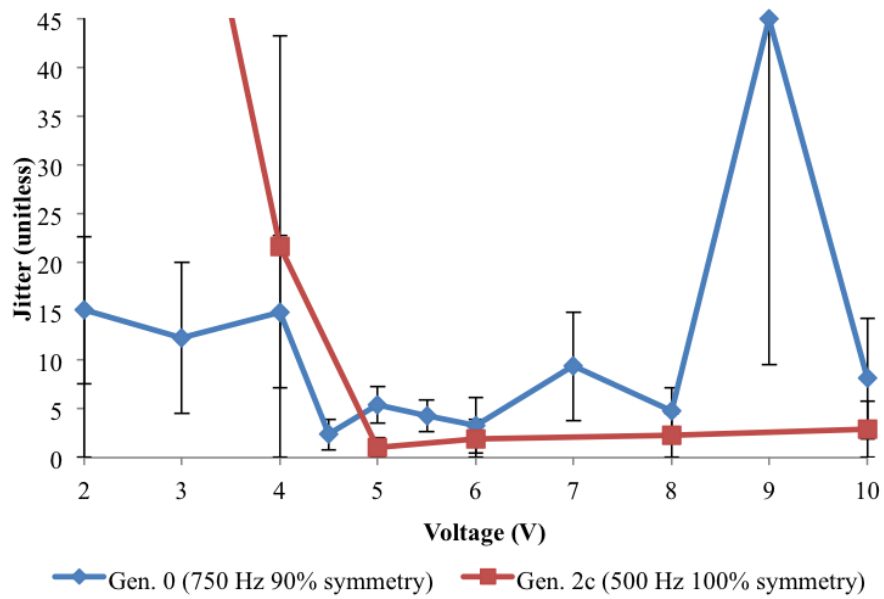


Figure 3.11: The jitter response to voltage amplitude variation shows a good region of operation between 5 V and 8 V, as well as at 10 V. The discrepancy at 9 V is likely due to issues placing the chip consistently on the surface.

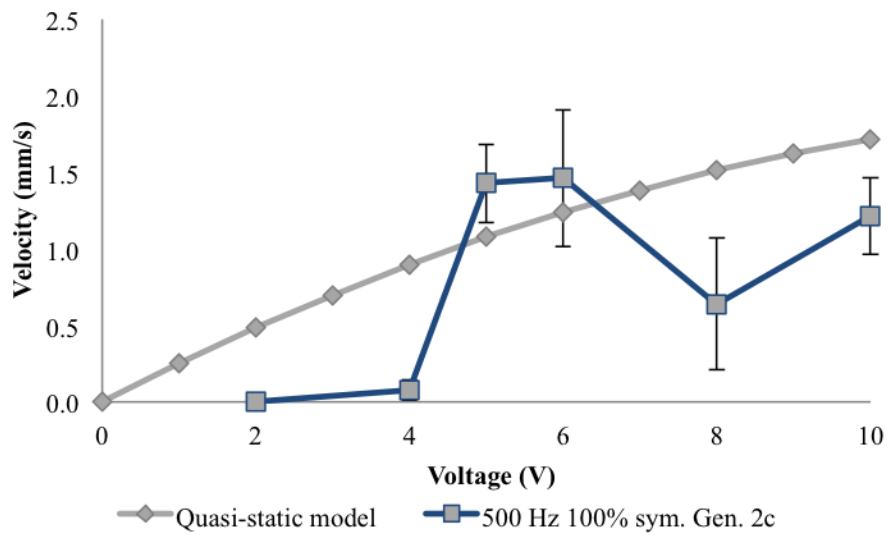


Figure 3.12: The quasi-static model predicts an increasing trend from 2 V to 10 V for 500 Hz and 100% ramp wave symmetry, but the experimental data shows that voltages lower than 4 V are not sufficient to induce displacement.

### 3.5 Frequency Results

Several frequency variation studies were performed on two generations of devices to assess the impact of frequency on velocity and DIE jitter. Figure 3.13 shows that the on-axis velocity response increases to a peak between 600 Hz and 900 Hz, and then each test experiences some decrease in on-axis velocity at higher frequencies near 1000 Hz. Likely this is due to the onset of resonance that interfere with the hopping mechanism at high frequency actuation and create less stable motion. The DIE jitter values, shown in Figure 3.14 also support this, with the lowest jitter values for all four tests between 500 Hz and 900 Hz. The frequency variation testing gives an idea of the range of frequencies most likely to produce rapid and reliable motion and demonstrates the sensitivity to frequency of actuation of these actuator surfaces.

Experiments varying excitation frequency show that device behavior is highly sensitive to the frequency of operation. Because frequency was observed to have a complex effect on velocity, the experimental results were compared to both the quasi-static and the dynamic model.

Both models generally predict that increased frequency will lead to increased velocity, as the total motion is essentially a summation of the hop displacements caused by each cycle of actuation. The increasing trend can be seen clearly in the quasi-static model in Figure 3.15. Figure 3.16 illustrates the agreement between the dynamic model and the experimental values. The qualitative agreement between the dynamic model and the experimental results suggests that many of the

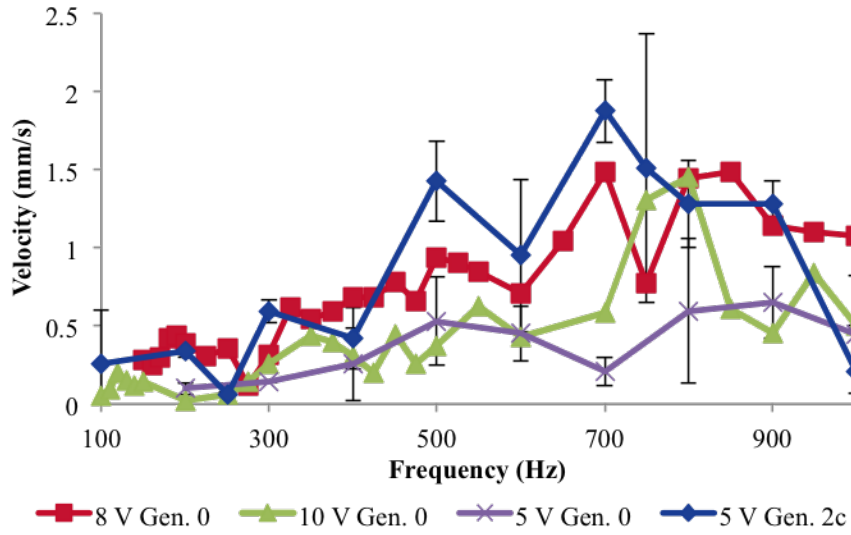


Figure 3.13: The highest on-axis velocities are achieved between 600 and 900 Hz. The lower bound reflects the necessity for the repetition of “hops” and the upper bound reflects the onset of resonance

contributing parameters in the dynamic model, like actuator ringing and contact transition behavior, influence the deviation from the quasi-static model.

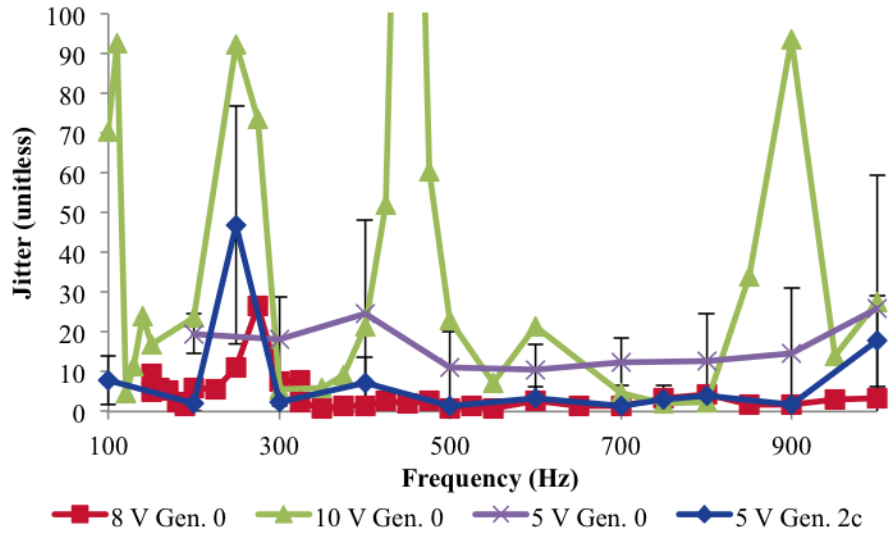


Figure 3.14: The jitter values for all four experimental sets is between 500-900 Hz. This falls between the lower frequencies that produce consistent forward motion and the onset of resonance.

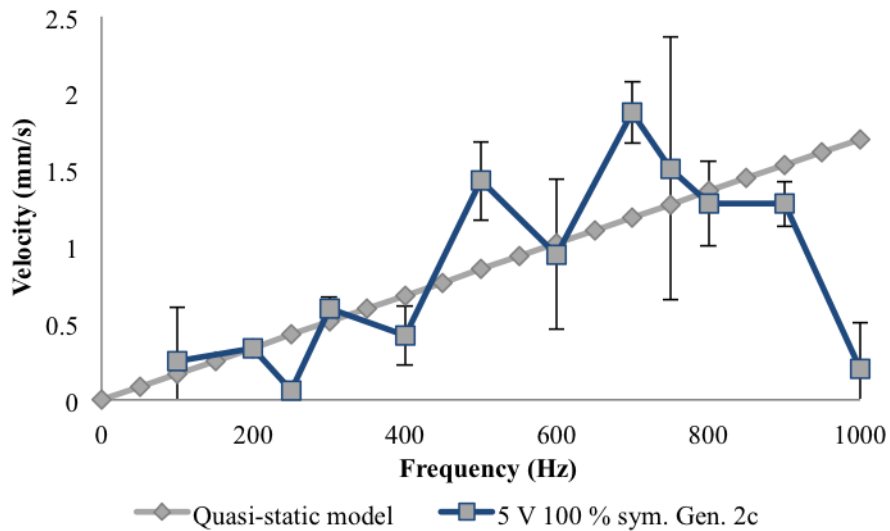


Figure 3.15: The quasi-static model shows a similar trend to the 5 V experimental data except at high frequencies where resonance creates dynamic effects not accounted for by the quasi-static model.

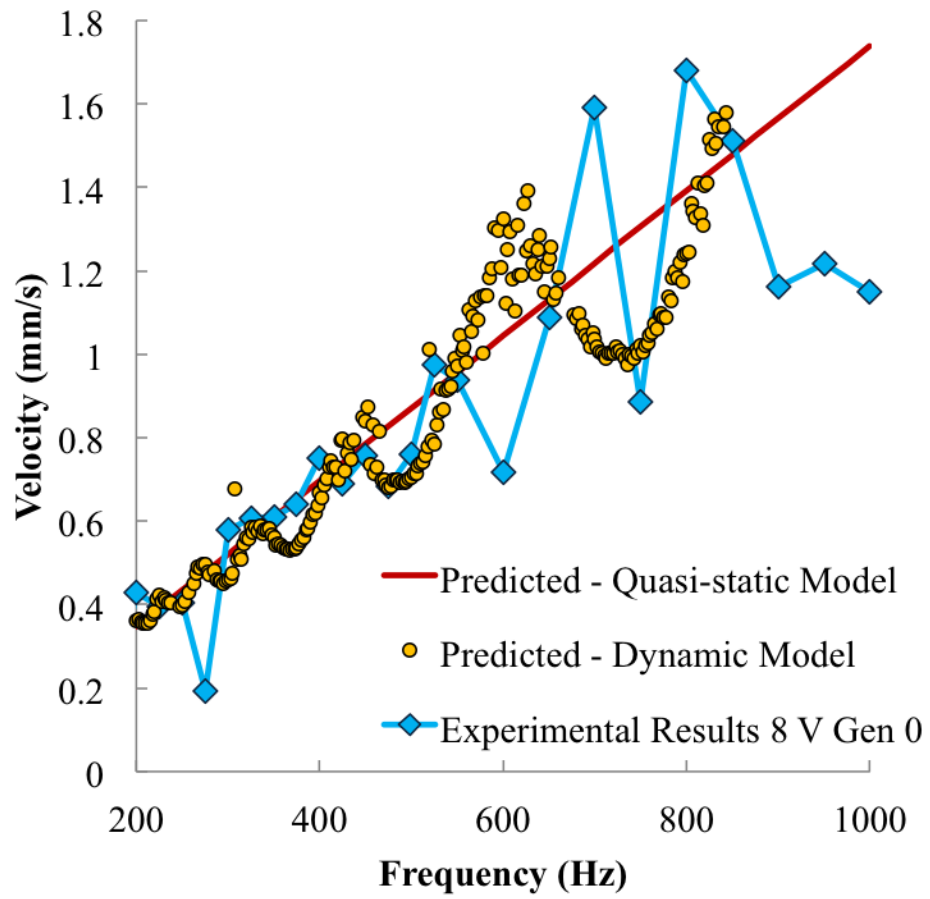


Figure 3.16: The multi-physics model agrees qualitatively with the experimental data from an 8 V ramp wave 100% symmetry test of a Gen. 0 device.

## 3.6 Actuator Length and Width Results

In addition to the three actuation signal parameters that were studied, the length and width of the piezoelectric actuator were varied as well to optimize the design going into the fourth generation of devices. In order to observe the affect of actuator length and width on motion, the third generation of devices was designed to have two widths (8  $\mu\text{m}$  and 16  $\mu\text{m}$ ) and six lengths (15  $\mu\text{m}$ , 32  $\mu\text{m}$ , 52  $\mu\text{m}$ , 72  $\mu\text{m}$ , 92  $\mu\text{m}$ , and 112  $\mu\text{m}$ ). Unidirectional and bidirectional surfaces were tested.

### 3.6.1 Length

Because the quasi-static model predicts that longer actuators will lead to larger on-axis velocities, a parametric study of the length of the actuators was performed. The on-axis velocity response to length variation, shown in Figure 3.17, demonstrates that longer actuators are generally better at producing higher velocities. The separation into unidirectional and bidirectional experimental sets simply indicates the array configuration used in the test. The frequencies and voltages of these tests were: 1000 Hz and 10 V for the 15  $\mu\text{m}$  long actuators, 200 Hz and 10 V for 32  $\mu\text{m}$  long, 200 Hz and 8 V for 52  $\mu\text{m}$  long actuators, 500 Hz and 2 V for 72  $\mu\text{m}$  long, 100 Hz and 4 V for 92  $\mu\text{m}$  long, and 150 Hz and 5 V for 112  $\mu\text{m}$  long. These values were determined qualitatively to be low-jitter, high-velocity operating conditions for each length. The operating conditions vary significantly between lengths because the actuator must provide enough vertical deflection (through voltage) to overcome adjacent posts in the array and must also stay below the resonant frequency of the

actuators, which is lower for longer actuators. A balance must be struck between the potential for increased speed through raising voltage and frequency and the potential for unstable motion at high voltages and frequencies. The DIE jitter response shows that motion is also smoother for actuator lengths above  $72 \mu\text{m}$  as seen in Figure 3.18. The two lengths that are most promising for both speed and jitter are  $72 \mu\text{m}$  and  $112 \mu\text{m}$ .

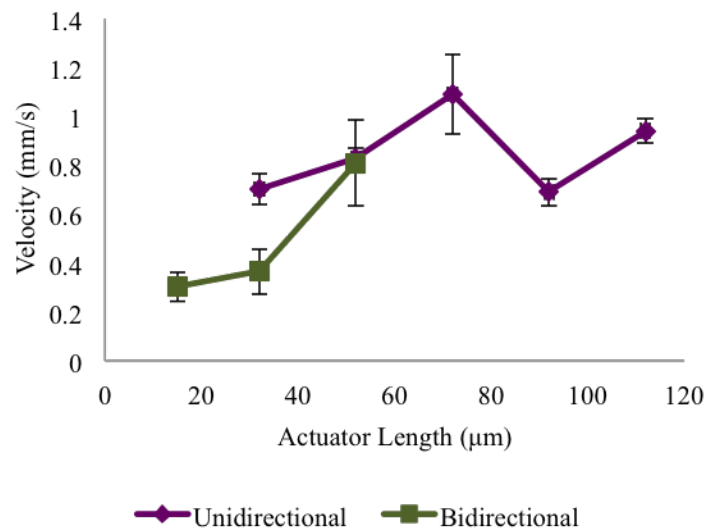


Figure 3.17: With the length data separated into unidirectional and bidirectional experimental sets, the on-axis velocity can be generally seen to increase with actuator length.

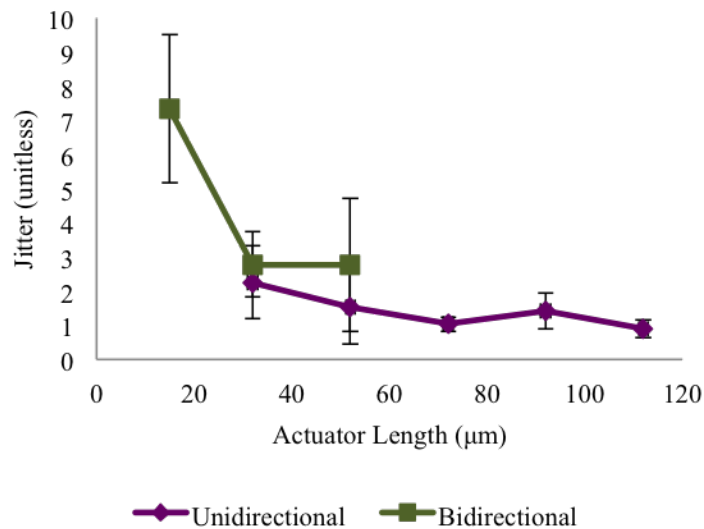


Figure 3.18: The separate unidirectional and bidirectional length studies both show decreasing jitter with increasing actuator length.

### 3.6.2 Width

Two widths of actuators were evaluated:  $8 \mu\text{m}$  and  $16 \mu\text{m}$ . A trade-off was anticipated between the two widths. If a larger number of more compliant (smaller width) actuators per component area leads to a greater number of actuator-component contacts, smoother motion is anticipated. However, if the number of actuator-component contacts is largely independent of the actuator stiffness, wider actuators should increase resonant frequencies of the actuator-component system, allowing higher frequencies of operation of the system. The results, shown in Figures 3.19 and 3.20, show that, in fact, the  $16 \mu\text{m}$  actuators have better performance for both on-axis velocity and DIE jitter.

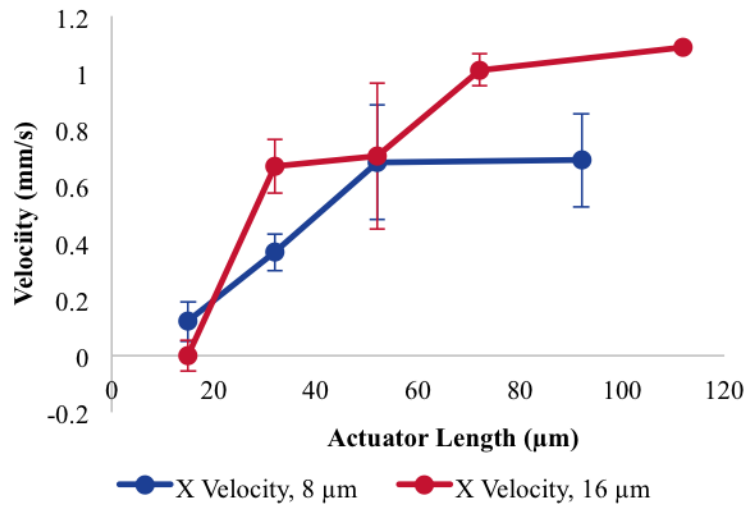


Figure 3.19: 16  $\mu\text{m}$  wide actuators are capable of achieving higher on-axis velocities than 8  $\mu\text{m}$ . This test was performed at 200-1000 Hz and 8-10 V depending on the length of actuator to obtain low-jitter motion.

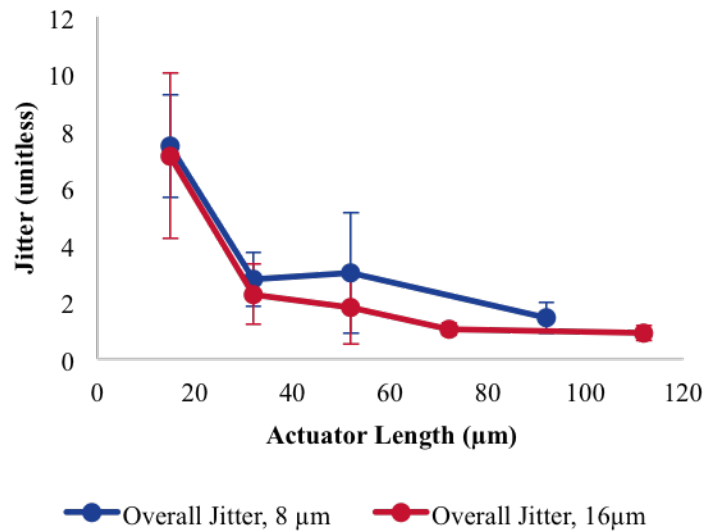


Figure 3.20: For 8  $\mu\text{m}$  and 16  $\mu\text{m}$  wide actuators, the jitter response is very similar. This indicates that actuator width does not affect the quality of motion as much as actuator length does.

## 3.7 Technical Challenges

While performing the initial voltage amplitude and frequency testing, two technical challenges emerged: chip motion stalls and non-center-of-mass rotations. In some tests, chips would advance across the array and then stop, sometimes temporarily, sometimes permanently. Unpredictable stalling behavior seriously damages the capability of open-loop operation. If a stall is permanent, it could completely disable closed-loop control of component positioning. Another issue was non-center-of-mass rotations, which cause rotational jitter and off-axis jitter when the center of rotation is time-varying.

### 3.7.1 Side Contact

It was hypothesized that stalls were a result of side contact between posts and chips, with the chips unable to overcome the large in-plane stiffness of the actuators. To investigate side contact, high-speed videos were taken of a stalled chip on a first generation device. As seen in Figure 3.21, side contact was in evidence. It was demonstrated that up to 1 kHz, this side contact could prevent the chip from further progress. Non-COM rotations were also observed with a center of rotation at the edge of the chip, suggesting side contact.

### 3.7.2 Post Height Variation

Non-COM rotations were theorized to be a result of frictional discrepancies caused by post-height variation. If the chip was losing contact with the posts asyn-

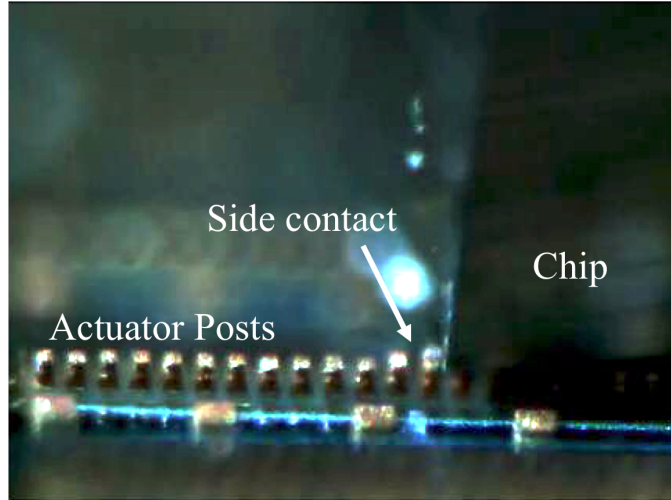


Figure 3.21: This image shows an example of side contact between a copper post and the silicon chip that prevented this chip from advancing, even at frequencies of 1 kHz.

chronously, its inertia could cause it to rotate around the last contact(s) it remained in contact with. Examining post height variation required SEM and confocal microscopy.

SEM of the array showed that large variations in post formation existed across the array, from over-etched to under-etched to mushrooming copper layers as shown in Figure 3.22. Using confocal microscopy, post heights were measured across the array. Confocal microscopy revealed variations of up to  $2.5 \mu\text{m}$  across the Gen. 0 device. In Gen. 2, the posts were changed to gold in order to have more uniform post heights and smoother metal surfaces. The Gen. 2 fabrication process had a poor yield, so in Gen. 3, copper posts were used, but the wet etch used to remove the photoresist mold and copper seed layer were replaced with an oxygen plasma and ion milling process to reduce the etching of the copper posts. The process change

resulted in more uniform posts than in Gen. 0 and Gen. 1. Compared to Gen. 0, the Gen. 3 parts had half as much variation between post heights. Gen. 3 parts had fewer issues with stalling and non-center-of-mass rotations, and this process change was a significant factor in the improved performance.

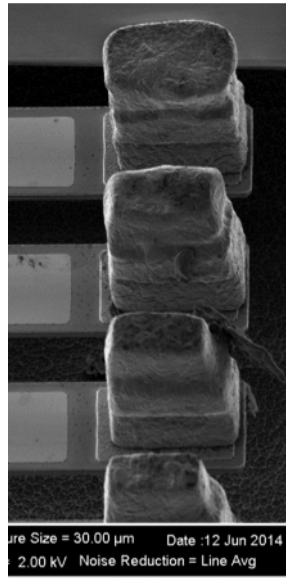


Figure 3.22: This SEM of a Gen. 1 device’s posts shows over-etch of the metal at the bottom and mushrooming at the top.

### 3.8 Jitter Improvement

The actuator surface motion capabilities have improved over design generations. More recent generations of devices are consistently more precise, largely due to improved fabrication results and parametric controls (i.e. voltage amplitude, frequency, and waveform). In order to demonstrate this improvement, the performance of experiments from four generations (Gen. 0, Gen. 1, Gen. 2, and Gen. 3) were evaluated to find the per-generation average jitter and the minimum per-experiment

average jitter. Then the average values were plotted as a bar graph and the best values were plotted as a line graph in Figure 3.23.

First generation device trials resulted in a per-generation average DIE jitter value of 17.16 and the most recent device trials have an average of 2.95 DIE jitter value. Gen. 1 parts show the poorest average performance. Gen. 3 parts show the best performance in terms of both average jitter value and minimum per-experiment jitter. The precision and reliability of motion on the RFactory actuator surface has improved as new generations of devices have been designed, fabricated, and tested.

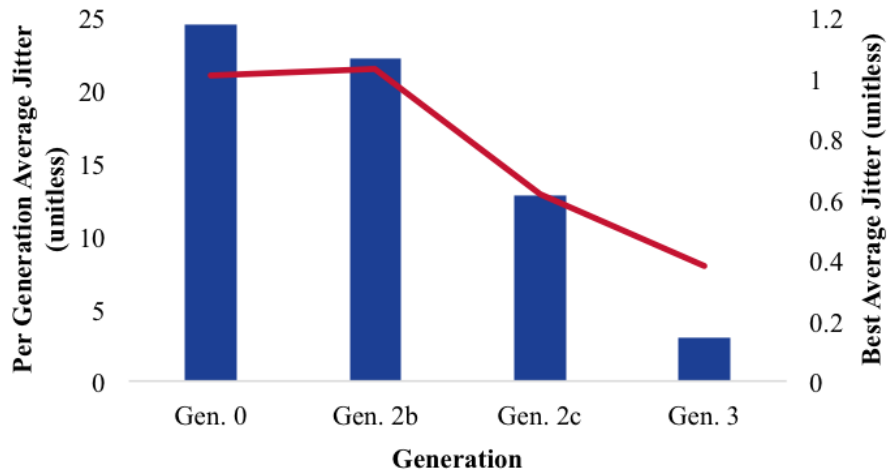


Figure 3.23: The blue bars show the average DIE jitter for tests from Gen. 0 through Gen. 3. Logically the average jitter should decrease over time as the operating conditions are improved. The minimum per-experiment average DIE jitter has also been included on the red line, showing that the minimum achievable jitter has improved over time.

### 3.9 RFactory System Demonstration

The actuator surface and interconnect substrate subsystems were integrated as shown in Figure 3.24 to demonstrate overall system feasibility. The key features of a reconfigurable circuit, namely the ability to move an arbitrary component into the desired position and the connection and disconnection of the chosen component were demonstrated under open-loop control. Bidirectional translation surfaces (+/- X) were utilized to align, separate, and reconnect the DC component chips. As part of the initial system level demonstrations of DC reconfiguration, +/- X translation surfaces were operated 14 times with 12 successful relocations of the component chip to the contact area. For all successful tests, the contact resistance was less than 500 m $\Omega$ . These initial tests were performed using 1 mm  $\times$  1 mm silicon chips with a bumped gold trace to close the circuit, seen in Figure 3.25. Additional tests, such as the one shown in Figure 3.26 have successfully connected and disconnected one 1.57 GHz SAW filter with only 0.2 dB additional insertion loss. The RF filter connection was confirmed, as seen in Figure 3.27. The piezoelectric actuator array can successfully manipulate milli-scale parts for DC and RF reconfigurability.

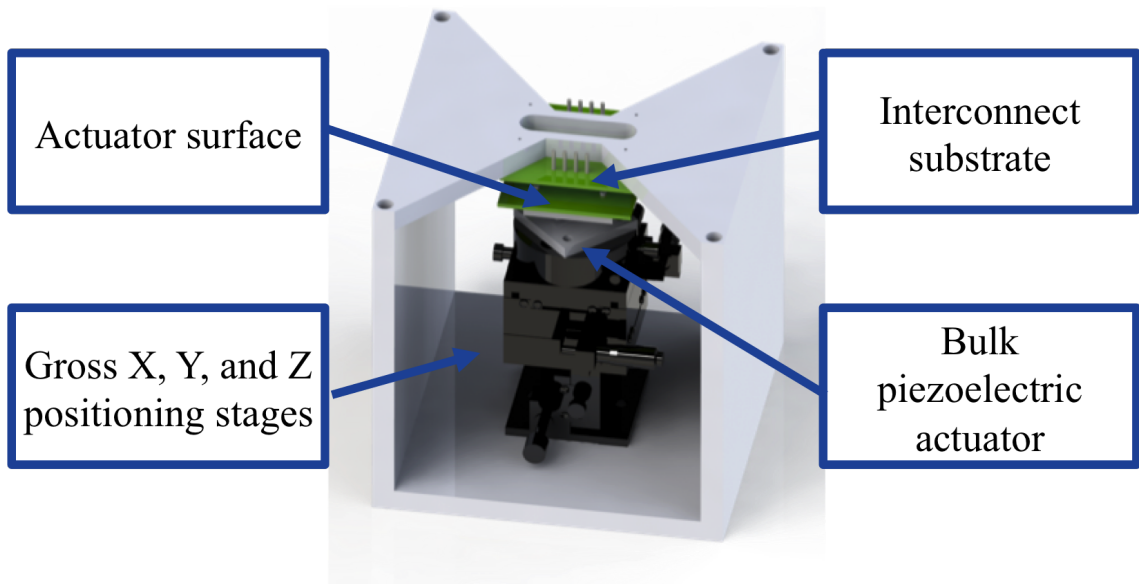


Figure 3.24: This illustration of the RFactory assembly shows the housing that contains the actuator surface, the bulk piezoelectric actuator, and the electrical interconnect surface.

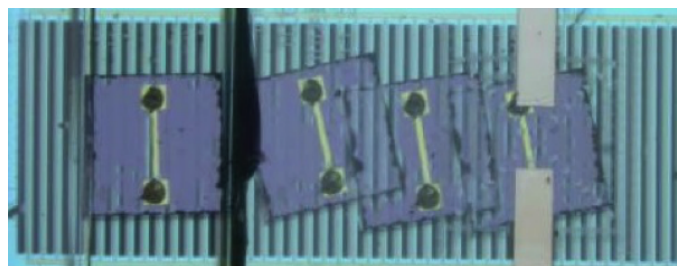


Figure 3.25: This time-lapse overlay image shows the progress of a DC component chip as it moves into place on the actuator surface.

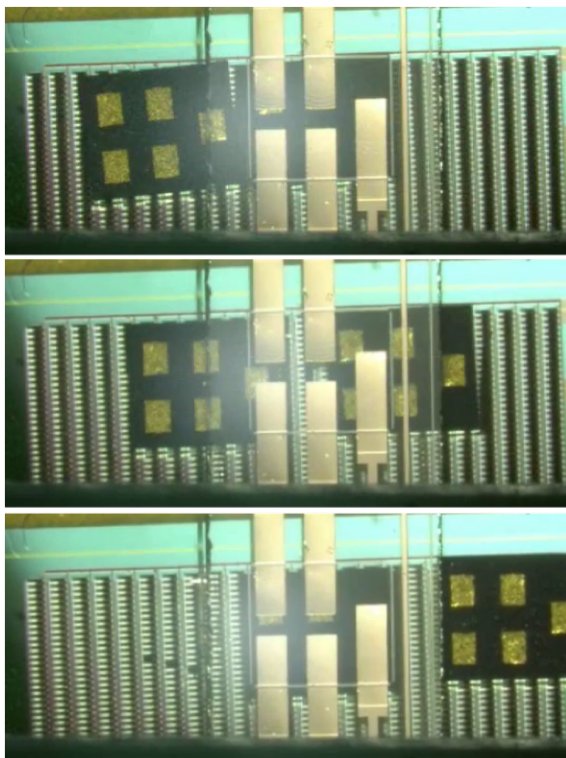


Figure 3.26: These images, from top to bottom, show a 1.57 GHz SAW filter being exchanged for a 1.18 GHz SAW filter on the RFactory actuator surface.

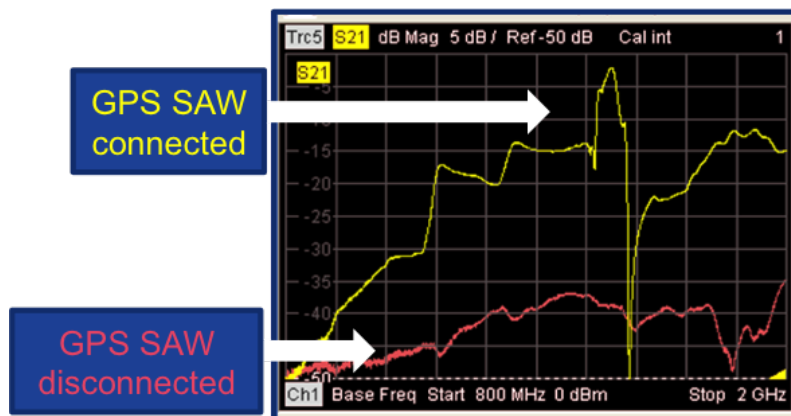


Figure 3.27: The output of the vector network analyzer shows that RFactory can successfully connect an RF filter, as seen by the  $<2\text{dB}$  attenuation in the passband when the filter is attached compared to the rejection seen when the filter has been unattached.

## Chapter 4: Conclusions and Future Work

A piezoelectric MEMS actuator array has been designed, fabricated, and characterized to address the micro-scale manipulation requirements of a motion-enabled reconfigurable RF circuit factory, known as RFactory. The author:

- Investigated physics of operation and contributed to modeling of system dynamics via FEA
- Experimentally characterized the impact of multiple parameters on on-axis velocity and jitter
- Improved the quality of motion through design, process modification, and operating condition refinement
- Demonstrated basic RFactory circuit reconfiguration functionality

These contributions were incorporated, in part, into the following publication:

Tellers, Mary, et al. “Piezoelectrically Actuated Arrays for Motion-Enabled Reconfigurable RF Circuits.” 18th International Conference on Solid-State Sensors, Actuators, and Microsystems (Transducers 2015). Alaska, USA, Jun. 21-25 2015.

Two models were developed to examine the physics of operation of the actuator surface. The first model, a quasi-static model, simplified the motion to constant

unidirectional translation based on the peak actuator velocities. The second model, a multi-physics dynamic model, assembled dynamic effects such as ringing and modal transitions with micro-scale phenomena like friction-modulated adhesion and air-damping. This more cohesive model demonstrated the effects of the hypothesized physics of operation and clarified the experimental deviation from the quasi-static predicted behavior.

In comparison to previous work in micro-manipulation, shown in Table 4.1, RFactory’s actuator arrays demonstrated higher translational velocities than both electro-thermal and electrostatic actuation [1, 10]. The rotation achieved by RFactory was three orders of magnitude higher than the rotation achieved through electro-thermal actuation [10]. The RFactory actuator surface demonstrates the competitiveness of piezoelectric actuator arrays as a micromanipulation mechanism.

Table 4.1: Comparison of RFactory to Previous Micromanipulation Results

<b>Actuation Mechanism</b>	<b>Maximum Translational Velocity (mm/s)</b>	<b>Maximum Rotational Speed (RPM)</b>
<b>Piezoelectric (RFactory)</b>	4.0	31
<b>Electro-thermal [10]</b>	.25	.006
<b>Electrostatic [1]</b>	.2	N/A
<b>Distributed Air-flow [15]</b>	8.3	N/A
<b>Diamagnetic Levitation [16]</b>	375	N/A

Four generations of devices were fabricated and tested with the ultimate goal of improving motion quality and speed of components across the array. The parameters that were varied in experimentation were: waveform, voltage amplitude, frequency, actuator length, and actuator width. In order to easily quantify the motional noise of the system, a metric known as distance interval error jitter was created and normalized to project objectives. Additionally, the on-axis velocity was a key metric in assessing the quality of motion achieved by the components on the actuator surface. The ranges of operating conditions in which the on-axis velocity and DIE jitter performance are greater than 1 mm/s and less than 2, respectively, are summarized in Table 4.2.

Table 4.2: Good Operating Conditions

Parameter	Value or Range for Good Operation
Waveform	Ramp wave, 100% symmetry
Voltage Amplitude	>5 V
Frequency	500-900 Hz
Actuator Length	72 and 112 $\mu\text{m}$
Actuator Width	16 $\mu\text{m}$

The next steps in the RFactory actuator surface project are to reconfigure more than just two components and to move to closed-loop control. Several things must be achieved in order to demonstrate more flexibility in reconfiguration. First, actuator surfaces enabling +/- XY motion must be tested and optimized. Rotation stages may be useful in addition to +/- XY translational arrays in order to correct

for rotation at the contact locations. Next, in order to enable fully heterogeneous integration, a standard thickness will be established for all components, with thinner components being placed on an intermediary layer to account for height differences. This material will be in contact with the actuator posts, so the choice of material for this gap material should be studied comprehensively. Finally, more work remains to be done in seamlessly integrating the electrical interconnect substrate and the actuator surface. In order to move to closed-loop control, capacitive sensors developed concurrently to the actuator surface must be integrated into the actuator surface [27]. With the position sensing enabled by the mutual capacitance sensing electrodes, the precision and speed of RFactory's actuator can be improved. Closed-loop control will allow for corrections to deviations. In addition, the alignment of the components with the electrical connections can be more reliable than the optical alignment previously used. Improved alignment will enhance the RF performance of the reconfigured circuits. With additional components to reconfigure and closed-loop control, RFactory could be implemented in laboratory applications for testing electronic components without having to wire-bond.

The RFactory actuator surface has proven its basic functionality and its tunability using waveform parameters and design variables. What remains is to expand its use, improve its functionality, and increase its component count.

## Appendix A: MATLAB Motion Tracking Code

```
close all
clear all

%Read video in, crop for calibration, choose marker points, track motion

%Each of these need to be adjusted for each voltage and frequency and crop
%width

str3 = '8v_new1';%file to save to (excel and avi
xRange = 'b2';%tells it what column to write data to
title_range = 'b1';%tells it to write the filename to the top of the column
pixcrop = 500;%1000 for big chip size 500 for little chip
good = [523 573];%useful frame selection
thresh = 0.16;
blob = 25;

%automatic processes
str = input('What is the filename without any extension?', 's');
title1 = {str};
avi = '.avi';
xls = '.xls';
mat = '.mat';
avi1 = '\\Client\C$\Users\marytellers\Desktop\T2_1D 8V\results\';
xls1 = '\\Client\C$\Users\marytellers\Desktop\T2_1D 8V\';

filename = [str avi];
filename1 = [xls1 str3 xls];
filename2 = [avi1 str avi];
matname = [xls1 str mat];

readerobj = VideoReader(filename);
numFrames = get(readerobj, 'NumberOfFrames');
vidFrames = read(readerobj, good);
nFrames = good(2)-good(1);
```

```

%
%
% %%
% %convert the frames to images
get(readerobj);
last = read(readerobj,good(2));
first = read(readerobj,good(1));
second = read(readerobj,(good(1)+1));

%first = imread('f1.png');%temp command for jpg file
%to crop image and calibrate to micron size
image(first)
title('Pick 2 corners of the chip')
[d,e] = ginput(2);
image(first)
title('Pick crop points left to right')
[a,b] = ginput(2);
%BW = imrotate(first,atan2(b(2)-b(1),a(2)-a(1))*180/pi);%straightens out
%the image...not always
rect = [a(1) 10 a(2)-a(1) b(2)-10];
%crop first and last to match
%last = imcrop(l1, rect);
f1 = imcrop(first, rect);
l1 = imcrop(last, rect);
[d1,d2,d3] = size(f1);

%set sizes of all matrices to be populated
EE = ones(d1,d2,good(2)-good(1));
%DD = zeros(28,2,good(2)-good(1));%figure out size better for saving centroid pos
FF = zeros(d1,d2,91);
%coordinates = zeros(3,2,good(2)-good(1));
X1a = ones(d1,d2,good(2)-good(1));
X1 = ones(d1,d2,good(2)-good(1));
traj = zeros(good(2)-good(1),2);
F = ones(d1,d2,good(2)-good(1));
I = zeros(good(2)-good(1),1);
HH = ones(2,4,good(2)-good(1));
vv = zeros(1,1,91);

imshow(f1);
str1 = 'pick vertices clockwise from top left';
title(str1,'Color','r','FontSize',12);
[mX, mY, chip, mx, my] = roipoly;

writerObj = VideoWriter(filename2);

```

```

writerObj.FrameRate = 5;
open(writerObj);

imshow(f1)
axis tight
set(gca,'nextplot','replacechildren');
set(gcf,'Renderer','zbuffer');

for k = good(1):good(2);

    X1a = read(readerobj,k);
    se=strel('disk',blob);
    X2 = imcrop(X1a, rect);
%    X3 = rgb2gray(X2); %one of the options for highly reflective but not well-f
%    firstX = im2bw(X3,.85);

    X1 = rangefilt(X2);
    firstX = im2bw(X1,thresh); %convert to bw to find centroids
    first2 = imclose(firstX,se);
    first1 = bwareaopen(first2,1000);
    EE(:,:,k-(good(1)-1))=first1;
    j = k-(good(1)-1);
    s = regionprops(first1,'Area','Centroid','Eccentricity','Orientation');
    centroids = cat(1, s.Centroid);
    areas = cat(1,s.Area);
    eccentric=cat(1,s.Eccentricity);
    orient=cat(1,s.Orientation);
    r=size(areas);
    ind = zeros(size(areas));
    ind2 = zeros(size(areas));
    centroids3 = zeros(size(centroids));
    centroids4 = [0,0];
    centroids2 = [0 0];
    for tt= 1:r(1,1);
        B = areas(tt,1)>=7000;
        A = eccentric(tt,1)<=.66;
        ind(tt,1)= A & B;
        centroids3(tt,1) = ind(tt,1)*centroids(tt,1);
        centroids3(tt,2) = ind(tt,1)*centroids(tt,2);
    end
    if size(centroids3)==[1,2];
        centroids2 = centroids;
    else
        centroids4=nonzeros(centroids3);
        centroids2(1,1)= centroids4(1,1);

```

```

        centroids2(1,2)= centroids4(2,1);
    end
    no_cent = sum(ind);
    %JJ(k,:)=no_cent; %saves number of centroids for checking later
    traj(k-(good(1)-1),:)= centroids2; %saves the centroid locations

l1 = sqrt((mx(1)-mx(4))^2+ (mx(1)-mx(4))^2);
l2 = sqrt((mx(1)-mx(2))^2+ (mx(1)-mx(2))^2);
aa = sqrt((l1^2+l2^2))/2;

for theta = 1:901
    deg = theta-1;%note that theta is actually orientation +1 degree
    acx = traj(k-(good(1)-1),1)-(aa*cos(deg*pi/1800));%this calculates the ver
    bcx = traj(k-(good(1)-1),1)+(aa*sin(deg*pi/1800));
    dcx = traj(k-(good(1)-1),1)+(aa*cos(deg*pi/1800));
    ecx = traj(k-(good(1)-1),1)-(aa*sin(deg*pi/1800));
    acy = traj(k-(good(1)-1),2)-(aa*sin(deg*pi/1800));
    bcy = traj(k-(good(1)-1),2)-(aa*cos(deg*pi/1800));
    dcy = traj(k-(good(1)-1),2)+(aa*sin(deg*pi/1800));
    ecy = traj(k-(good(1)-1),2)+(aa*cos(deg*pi/1800));
    c = [acx bcx dcx ecx];
    r = [acy bcy dcy ecy];
    FF(:, :, theta)= roipoly(first1,c,r);
    vv(:, :, theta) = sum(sum(abs(EE(:, :, k-(good(1)-1))-FF(:, :, theta))));%finds the
    [C,I(k-(good(1)-1),:)] = min(vv);
    %GG(:, :, k) = abs(DD(:, :, k)-FF(:, :, I(k, :)));
    acxx = traj(j,1)-(aa*cos((I(j)-1)*pi/1800));%this calculates the vertices
    bcxx = traj(j,1)+(aa*sin((I(j)-1)*pi/1800));
    dcxx = traj(j,1)+(aa*cos((I(j)-1)*pi/1800));
    ecxx = traj(j,1)-(aa*sin((I(j)-1)*pi/1800));
    acyy = traj(j,2)-(aa*sin((I(j)-1)*pi/1800));
    bcyy = traj(j,2)-(aa*cos((I(j)-1)*pi/1800));
    dcyy = traj(j,2)+(aa*sin((I(j)-1)*pi/1800));
    ecyy = traj(j,2)+(aa*cos((I(j)-1)*pi/1800));
    HH(1, :, k) = [acxx bcxx dcxx ecxx];
    HH(2, :, k) = [acyy bcyy dcyy ecyy];
end

figure
imshow(first1)
    hold on
    plot(centroids2(:,1), centroids2(:,2), 'r*')
    plot(HH(1, :, k), HH(2, :, k), '-ro', 'MarkerEdgeColor', 'k', 'MarkerFaceColor', 'yellow')
    plot(traj(:,1), traj(:,2), 'm*')

```

```

vid(k-(good(1)-1)) = getframe(k-(good(1)-1)+1);% why k+1? i forget
writeVideo(writerObj,vid(k-(good(1)-1)));

end

%write video, calculate pixfac, export to master file
%changed definition of X and Y so X is desired motion and Y is
%perpendicular motion
%movie(vid)

close(writerObj);
pixfac = pixcrop/sqrt((d(2)-d(1))^2+(e(2)-e(1))^2);
%pixfac=4.66;
traj1 = traj*pixfac;

%export position (pix values)
xlswrite(filename1,title1,'Y Position',title_range);
xlswrite(filename1,traj1(:,1),'Y Position',xRange);
xlswrite(filename1,title1,'X Position',title_range);
xlswrite(filename1,traj1(:,2),'X Position',xRange);

%plot and export angle

orientation= (I-1)/10 ;
% plot(orientation);
% axis([0 good(2)-good(1) 0 90]);
xlswrite(filename1,title1,'Orientation', title_range)
xlswrite(filename1,orientation,'Orientation', xRange);

save(matname,'-v7.3');
beep
movie(vid)

```

## Bibliography

- [1] K.-F. Bohringer, J.W. Suh, B.R. Donald, and G.T.A. Kovacs. Vector fields for task-level distributed manipulation: experiments with organic micro actuator arrays. In , *1997 IEEE International Conference on Robotics and Automation, 1997. Proceedings*, volume 2, pages 1779–1786 vol.2, April 1997.
- [2] Bruce Alan Fette. *Cognitive radio technology*. Academic Press/Elsevier, Amsterdam; Boston, 2009.
- [3] Ezio. Biglieri. *Principles of cognitive radio*. Cambridge University Press, Cambridge ;, 2012.
- [4] Lawrence J. Kushner, Douglas S. Jansen, Gregory M. FLewelling, Joseph D. Cali, Curtis M. Grens, Steven E. Turner, Kevin W. Slicch, Timothy Dresser, Mark E. Stuenkel, and Joseph Wood. MATRICs (Microwave Array Technology for Reconfigurable Integrated Circuits). GOMACTech, 2014.
- [5] Mike Lee, Mike Lucas, Robert Young, Robert Howell, Pavel Borodulin, and Nabil El-Hinnawy. RF FPGA for 0.4 to 18 GHz DoD Multi-function Systems. Technical report, DTIC Document, 2013.
- [6] Troy Olsson. Adaptive RF Technologies (ART).
- [7] Happy Henri, Gonzague Six, Matthieu Vanmackelberg, Alain Cappy, and Gilles Dambrine. Ultra low loss transmission lines on low resistivity silicon substrate. In *Microwave Symposium Digest. 2000 IEEE MTT-S International*, volume 3, pages 1809–1812. IEEE, 2000.
- [8] Jeffrey S. Pulskamp, Ronald G. Polcawich, Ryan Q. Rudy, Sarah S. Bedair, Robert M. Proie, Tony Ivanov, and Gabriel L. Smith. Piezoelectric PZT MEMS technologies for small-scale robotics and RF applications. *MRS Bulletin*, 37(11):1062–1070, November 2012.
- [9] Piezoceramic Materials & Properties.

- [10] J.W. Suh, R.B. Darling, K.-F. Bohringer, B.R. Donald, H. Baltes, and G.T.A. Kovacs. CMOS integrated ciliary actuator array as a general-purpose micromanipulation tool for small objects. *Journal of Microelectromechanical Systems*, 8(4):483–496, December 1999.
- [11] Mason Terry, Joel Reiter, Karl F. Bhringer, John W. Suh, and Gregory TA Kovacs. A docking system for microsattellites based on MEMS actuator arrays. *Smart materials and structures*, 10(6):1176, 2001.
- [12] E.Y. Erdem, Yu-Ming Chen, M. Mohebbi, J.W. Suh, G.T.A. Kovacs, B.B. Darling, and K.F. Bohringer. Thermally Actuated Omnidirectional Walking Microrobot. *Journal of Microelectromechanical Systems*, 19(3):433–442, June 2010.
- [13] M. Edo, Y. Watanabe, O. Morita, H. Nakazawa, and E. Yonezawa. Two-dimensional micro conveyer with integrated electrostatic actuators. In *Twelfth IEEE International Conference on Micro Electro Mechanical Systems, 1999. MEMS '99*, pages 43–48, January 1999.
- [14] Kristofer J. Pister, Ronald Fearing, and Roger Howe. A planar air levitated electrostatic actuator system. In *Micro Electro Mechanical Systems, 1990. Proceedings, An Investigation of Micro Structures, Sensors, Actuators, Machines and Robots. IEEE*, pages 67–71. IEEE, 1990.
- [15] Y. Fukuta, Y-A. Chapuis, Y. Mita, and H. Fujita. Design, fabrication, and control of MEMS-based actuator arrays for air-flow distributed micromanipulation. *Journal of Microelectromechanical Systems*, 15(4):912–926, August 2006.
- [16] Ron Pelrine, Annjoe Wong-Foy, Brian McCoy, Dennis Holeman, Rich Mahoney, Greg Myers, Jim Herson, and Tony Low. Diamagnetically levitated robots: An approach to massively parallel robotic systems with unusual motion properties. In *Robotics and Automation (ICRA), 2012 IEEE International Conference on*, pages 739–744. IEEE International Conference on Robotics and Automation (ICRA),, 2012.
- [17] S. Pal and H. Xie. A process for fabricating robust electrothermal micromirrors with customizable thermal response time and power consumption. In *2011 International Conference on Optical MEMS and Nanophotonics (OMN)*, pages 157–158, August 2011.
- [18] Karl-Friedrich Bhringer, Bruce Randall Donald, and Noel C. MacDonald. Single-crystal silicon actuator arrays for micro manipulation tasks. In *Micro Electro Mechanical Systems, 1996, MEMS'96, Proceedings. An Investigation of Micro Structures, Sensors, Actuators, Machines and Systems. IEEE, The Ninth Annual International Workshop on*, pages 7–12. IEEE, 1996.

- [19] Karl F. Bohringer, Bruce R. Donald, Noel C. MacDonald, Gregory TA Kovacs, and John W. Suh. Computational methods for design and control of MEMS micromanipulator arrays. *Computational Science & Engineering, IEEE*, 4(1):17–29, 1997.
- [20] M V Berry and A K Geim. Of flying frogs and levitrons. *European Journal of Physics*, 18(4):307–313, July 1997.
- [21] M. D. Simon and A. K. Geim. Diamagnetic levitation: Flying frogs and floating magnets (invited). *Journal of Applied Physics*, 87(9):6200–6204, May 2000.
- [22] James Burrell. *Disruptive effects of electromagnetic interference on communication and electronic systems*. PhD thesis, George Mason University, 2003.
- [23] Ronald G. Polcawich and Jeffrey S. Pulskamp. Additive Processes for Piezoelectric Materials: Piezoelectric MEMS. In Reza Ghodssi and Pinyen Lin, editors, *MEMS Materials and Processes Handbook*, volume 1, pages 273–353. Springer US, Boston, MA, 2011.
- [24] Gabriel L. Smith, Jeffrey S. Pulskamp, Luz M. Sanchez, Daniel M. Potrepka, Robert M. Proie, Tony G. Ivanov, Ryan Q. Rudy, William D. Nothwang, Sarah S. Bedair, Christopher D. Meyer, and Ronald G. Polcawich. PZT-Based Piezoelectric MEMS Technology. *Journal of the American Ceramic Society*, 95(6):1777–1792, June 2012.
- [25] J. Baborowski. Microfabrication of Piezoelectric MEMS. In *Electroceramic-based MEMS: fabrication-technology and applications*, number 9 in The Kluwer international series in: Electronic materials: science and technology, pages 325–359. Springer Science+Business Media, New York, 2005.
- [26] Paul Muralt. PZT thin films for microsensors and actuators: Where do we stand? *Ultrasonics, Ferroelectrics, and Frequency Control, IEEE Transactions on*, 47(4):903–915, 2000.
- [27] Christopher Reilly. *MEMS Capacitive Sensing for Position Detection of Movable Objects*. PhD thesis, The George Washington University, January 2015.
- [28] Sarah S. Bedair, Jeffrey S. Pulskamp, Christopher D. Meyer, Manrico Mirabelli, Ronald G. Polcawich, and Brian Morgan. High-Performance Micromachined Inductors Tunable by Lead Zirconate Titanate Actuators. *IEEE Electron Device Letters*, 33(10):1483–1485, October 2012.
- [29] S.S Bedair, J.S Pulskamp, C.D Meyer, R.G Polcawich, and I.M Kierzewski. Modeling, fabrication and testing of MEMS tunable inductors varied with piezoelectric actuators. *Journal of micromechanics and microengineering : structures, devices, and systems.*, 24(9):095017, 2014.

- [30] Ryan Q. Rudy, Gabriel L. Smith, Don L. DeVoe, and Ronald G. Polcawich. Millimeter-Scale Traveling Wave Rotary Ultrasonic Motors. *Journal of Microelectromechanical Systems*, 24(1):108–114, February 2015.
- [31] Jeffrey S Pulskamp, Robert M Proie, and Ronald G Polcawich. Nano- and micro-electromechanical switch dynamics. *Journal of Micromechanics and Microengineering*, 24(1):015011, January 2013.
- [32] Structural: Chapter 3.